SOFT MAGNETIC MICROROBOTS FOR TARGETED DRUG DELIVERY

by

Nahrin Nowrose

A Dissertation

Submitted to the Faculty of Purdue University

In Partial Fulfillment of the Requirements for the degree of

Master of Science

School of Electrical and Computer Engineering

West Lafayette, Indiana

December 2019

THE PURDUE UNIVERSITY GRADUATE SCHOOL
STATEMENT OF COMMITTEE APPROVAL

Dr. Ramses V. Martinez, Co-Chair

School of Industrial Engineering

Dr. Zhongming Liu, Co-Chair

Department of Electrical and Computer Engineering

Dr. Joseph V. Rispoli

Department of Electrical and Computer Engineering

Approved by:

Dr. Dimitrios Peroulis

Head of the Graduate Program

Dedicated to my loving parents and amazing husband.

AKNOWLEDGMENTS

I would like to thank the people who were of great help during my time here at Purdue University.

- My supervisor, Dr. Ramses V. Martinez for his continuous support and guidance.
- My committee members, Dr. Zhongming Liu and Dr. Joseph V. Rispoli.
- My lab-mates: Debkalpa Goswami, Nikhil Dave, Aniket Pal, Marina Sala De Medeiros, and Behnam Sadri.
- My husband Abdullah Arafat for providing me continuous physical and mental support.

TABLE OF CONTENTS

LIST OF TABLES 6
LIST OF FIGURES 7
LIST OF ACRONYMS 9
ABSTRACT 10
1. INTRODUCTION 11
2. DESIGN AND FABRICATION OF SOFT MAGNETIC MICROROBOTS 14
2.1 Introduction 14
2.2 Fabrication of SMμRs 14
2.2.1 Enhancing the Traction of the Microrobots Adding Nanopatterns to their Surface 15
2.2.2 Alignment of Magnetic Particles in a Polymeric Matrix Using Global Fields 15
2.2.3 Laser Micromachining of SMμRs 16
2.3 Biocompatibility of the SMμRs 18
2.4 Scanning Electron Imaging 19
2.5 Cost of Fabrication 20
3. WIRELESS CONTROL OF SMμRs USING ROTATING MAGNETIC FIELDS 21
3.1 Inducing Tumbling Motion Using Rotating Magnetic Fields 21
3.2 Measurement of the Magnetic Field Intensity 23
3.3 Controlling the Tumbling Motion of SMμRs 25
3.3.1 Kinematic Analysis 27
3.4 Tumbling Locomotion in Obstacle-filled Environments 28
4. TARGETED DRUG RELEASE USING SMμRS 31
4.1 SMμR Navigation in Liquid Media 31
4.1.1 Dependence of the Magnetic Field Intensity on the Distance between Magnet and SMμR 32
4.1.2 Collapsing the Porous Layer of SMμRs Using Extended Magnetic Fields 34
4.2 Discrete and Continuous Drug Delivery Along Gastrointestinal Tissue 34
5. CONCLUSIONS AND FUTURE WORK 37
APPENDIX 38
REFERENCES 44
VITA 49

LIST OF TABLES

Table 2.1. Itemized cost of materials to fabricate a SMµR..... 20

LIST OF FIGURES

Figure 2.1. Schematic diagram of the fabrication process of SMµRs. (a) A mixture of PDMS, magnetic powder, and caster sugar is deposited on top of a polymeric grating. This grating will enhance the traction of the microrobots. (b) The mixture is kept over a magnet to align the magnetic particles along a preferential direction. (c) The mixture is cured and then sonicated to dissolve the sugar particles to create pores in its structure. (d) The open pores are filled with drug. I used blue dye to simulate drug. (e) The two layers are unmolded from polymeric grating. (f) The top layer is attached to the middle and bottom layers to get SMµRs. 17

Figure 2.2. Step-by-step fabrication of SMµRs. (a) PDMS, magnetic powder, and caster sugar are mixed together. (b) The mixture is spread over a polymeric grating to incorporate nanopatterns. (c) The polymeric grating is then placed over a permanent magnet to align the magnetic particles inside the mixture. (d) The mixture is cured and then sonicated to dissolve sugar particles..... 18

Figure 2.3. SEM image of polymeric grating. The pitch of the polymeric grating is 1.6 µm. 19

Figure 2.4. (a) SEM image of porous PDMS based on caster sugar template. (b) SEM image of a magnetic particle. The average diameter of the magnetic particles is 150 µm..... 20

Figure 3.1. (a) Photograph of the experimental setup used to actuate SMµRs. (b) Zoom-in showing the actuating magnet attached to the end of a DC motor shaft (underneath the white tape). (c) Schematic representation of the movable magnetic stage used to actuate SMµR *via* rotating magnetic fields. 22

Figure 3.2. (a) Photograph of the experimental setup used to measure the intensity of the magnetic field. (b) Zoom-in showing the actuating magnet, microrobot on the actuation platform and hall effect sensor. (c) Schematic representation of the orientation of the axes of hall effect sensor... 24

Figure 3.3. Sidewise tumbling locomotion of SMµR. (a) Schematic diagram of the structure of a SMµR capable of sidewise translation. (b) Superimposed frames showing the forward and backwards sidewise locomotion of a SMµR..... 25

Figure 3.4. Lengthwise tumbling locomotion of SMµR. (a) Schematic diagram of the structure of a SMµR capable of lengthwise translation. (b) Superimposed frames showing the forward and backwards lengthwise locomotion of a SMµR. 26

Figure 3.5. Superimposed frames showing the capability of SMµRs to follow a square-like path. 27

Figure 3.6. Kinematic analysis of a magnetic microrobot. I used MATLAB 2016a (Mathworks Inc.) Image Processing Toolbox™ to track the position of the center of mass (centroid) of the magnetic microrobot. 28

Figure 3.7. Superimposed frames showing the navigation of a SMµR through a 3D printed maze with obstacles of different sizes and pitches..... 29

Figure 3.8. (a) Profile of the obstacle threads perpendicular to the direction of the maze. (b) Dependence of the average speed of the SMµRs on the obstacle size and pitch, for different rotational frequencies of the actuating magnetic field. 30

Figure 4.1. Dependence of the locomotion speed of the SMµR in different media (air, water, and vegetable oil) on the rotational frequency of the actuating magnet. 32

Figure 4.2. Variation of the magnitude of magnetic field intensity, |B|, along the axis perpendicular to the surface of the rotating magnet as a function of the distance to the magnet. 33

Figure 4.3. Superimposed frames showing the sidewise locomotion and targeted drug delivery of SMµR in water. Colored arrows represent the direction and the module of the magnetic field. . 34

Figure 4.4. Superimposed frames showing the navigation of the SMµR (in the direction of the arrows) and the discrete and continuous drug delivery over gastrointestinal tissue using a SMµR. The color of the arrows represents the direction and the module of the magnetic field along the path of the SMµR. 35

Figure 4.5. (a) Topological reconstruction of the path of the SMµR along the gastrointestinal tissue shown in figure 4.4. (b) Intensity and rotational frequency of the magnetic field applied to translate and release the drug on the areas of the tissue marked in figure 4.4. 36

LIST OF ACRONYMS

SMµR	Soft Magnetic Microrobot
NdFeB	Neodymium Iron Boron
PDMS	Polydimethylsiloxane
IPA	Isopropanol
CD	Compact Disc
SEM	Scanning Electron Microscope
3D	Three Dimensional
DC	Direct Current
GI	Gastrointestinal
PCL	Polycaprolactone

ABSTRACT

Author: Nowrose, Nahrin. MSECE
Institution: Purdue University
Degree Received: December 2019
Title: Soft Magnetic Microrobots for Targeted Drug Delivery.
Committee Co-Chairs: Ramses V. Martinez, Zhongming Liu

Microrobots have a promising prospect to be used in healthcare and bioengineering applications due to their capability to gently access small and delicate body sites. Unfortunately, traditional materials used for the fabrication of microrobots are rigid, hindering safe operation due to the transfer of high stresses to the surrounding tissue. Additionally, traditional microrobots are often not biocompatible, which threatens the health of the patient if not properly retrieved. This dissertation describes the fabrication and actuation of small-scale (several micrometers in all dimensions) magnetic robots that are soft, biocompatible, and capable of moving over smooth and corrugated surface. Soft Magnetic Micro Robots (SMμRs) can carry payloads in their porous interior and release them using external magnetic inputs. SMμRs has therefore the potential to be used in a wide range of applications—including targeted drug release and remote biosensing and bio sampling—and access a number of difficult-to-reach sites in the human body, such as intestines or blood vessels. The structure of SMμRs consist of three thin layers: Two layers of polymer with embedded magnetic particles aligned along a preferential direction. One porous layer, in between the magnetic layers, where the SMμRs can accumulate and release payloads. SMμRs are small, light in weight, and fast and inexpensive to fabricate. Moreover, the manufacturing of SMμRs is compatible with large-scale production processes, facilitating their future commercial exploitation. Using external rotating magnetic fields, the position of the SMμRs can be controlled wirelessly *via* tumbling locomotion. We demonstrate two types of tumbling locomotion (length-wise and side-wise) as well as the possibility to release the internal payload of the SMμRs in a discrete or continuous manner using only changes in the intensity of the external magnetic field. We studied the performance of SMμRs under a variety of environmental conditions as well as their capability of overcoming obstacles.

1. INTRODUCTION

Small robots have facilitated the access to small, and intricate regions of the human body [1] such as blood vessels [2], the gastrointestinal (GI) tract [3], where traditional tethered medical devices struggle to navigate. There are two different approaches for designing and controlling such robots: i) On board approaches, where the small robot has all the components to operate autonomously integrated in its structure; ii) Off-board approaches, where the components of the robotic system are externally powered and actuated [4].

The capability of these small robots to carry payloads in their interior has made them good candidates for targeted drug delivery [5]. Using small-scale robots, doctors can release therapeutic substances at the targeted sites—such as wounded tissue—in a controlled manner improving healing times [4]. To release the payloads carried by these small robots there are two approaches: i) Automatic deployment, triggered by the presence of certain enzymes or caused by pH changes [6], [7] at the targeted site; ii) Externally activated delivery, using external stimuli, such as light, ultrasounds [8], [9], magnetic fields [6], [10], or temperature changes [5]. Magnetic fields are a popular actuation method for controlling microrobots [11] due to their relatively long range and simple control. Unfortunately, the use of global magnetic fields, does not allow the individual control of multiple microrobots [12].

Several approaches have been taken for targeted drug delivery such as nanoparticle-based drug delivery [13], [14], micro-robotic drug delivery [8], [10], [15]–[21], or pH-triggered drug delivery [6], [7], [22], [23]. Nanoparticles take advantage of their small size, multifunctionality to efficiently navigate through blood and tissues, enabling the localized delivery of drugs. Unfortunately, it is difficult to ensure that the drug payload carried by the nanoparticles is delivered only at the point of need and not all over their path to the targeted area [13]. Recent advances in micro robotics have enabled the creation of sub-millimeter robots capable of sensing force [24]–[26], crawling [27]–[31], swimming [32]–[34], climbing [35]–[37], rolling [38]–[42], walking [43]–[47], tumbling [48]–[51], and jumping over obstacles [35], [52]. When the size of the damage tissue is too large for one microrobot, a team of microrobots can facilitate the delivery of the required amount of drug to the site [4]. Microrobots are often too small to carry with them, at the

same time, several sensors and communication/control systems, making it necessary to co-ordinate microrobots with different functionalities as a team or *microrobotic swarm* [53]. These microrobotic swarms behave as a single distributed actuating and sensing system composed of several collaborative microrobots [54]. Unfortunately, to further develop microrobotic swarms, new control systems with reduced complexity and new microrobotic gaits capable of overcoming obstacles need to be developed.

There are several fundamental challenges still limiting the design, fabrication, and actuation of microrobots: Materials currently used to fabricate microrobots come in direct contact with biological fluids and hence, they need to be resistant to corrosion in biological environments to avoid irreversible malfunction. Additionally, microrobots operating inside the human body need to be soft, biocompatible or bioresorbable, multifunctional and compatible to existing fabrication processes whereas current materials used to fabricate microrobots are typically rigid, not biocompatible, and often have one single function. Moreover, mass production of these microrobots is also crucial for their future commercial use [4]. These challenges need to be addressed to ensure efficient biomedical application of microrobots.

Microrobots operating without any threads connected to them can move freely inside the body and are suitable for in vivo tissue inspection and sampling applications [55]. Magnetically-guided actuation enables wireless control of those microrobots, allowing for their precise actuation and control inside the body [56]. In this dissertation, I propose a scalable fabrication method to fabricate drug-loaded soft magnetic microrobot (SMµR) and a magnetic actuation method to remotely control the tumbling locomotion of the SMµRs and their targeted drug release. The resulting SMµRs are soft, small, lightweight, and capable of doing lengthwise and sidewise locomotion both in forward and backward directions. We demonstrate that SMµRs can navigate through flat, corrugated surfaces overcoming obstacles under various environmental conditions. The incorporation of nano texturized surfaces to SMµRs increases their adhesion with surface, enabling SMµR to move through viscous medium without slipping. The surface of the SMµRs is hydrophobic, which facilitates the reservation of drug payload. I also demonstrate that SMµRs can transport and release drug to specific locations of the body. Additionally, SMµRs offer several advantages as follows: (1) they do not cause any damage to the tissues due to high stresses as they

are soft; (2) they are fast and inexpensive to fabricate; using processes compatible with large scale production; (3) they are easily controllable using external rotating magnetic fields; (4) they can be readily eliminated from the body after use.

This dissertation is organized as follows: Chapter 2 describes the design and fabrication methods of soft magnetic microrobots. Chapter 3 contains the wireless actuation method for locomotion in various environments. Chapter 4 describes the method for targeted drug release. Finally, chapter 5 describes the summary of the project and future directions.

2. DESIGN AND FABRICATION OF SOFT MAGNETIC MICROROBOTS

2.1 Introduction

The manufacturing of micro and nanopatterns has led to the development of a variety of soft lithographic techniques, which use elastomeric stamps or molds to rapidly replicate patterns on a surface. Due to its simplicity and low cost, I used replica molding, a soft lithographic technique, to fabricate both the porous PDMS layer and the nanopatterns on the top and bottom surfaces of the SMµRs. Adding pores to the middle PDMS layer of the SMµRs provides them with empty reservoirs that can be used for the storage of payloads, while preserving their natural hydrophobicity, flexibility, and low cost. Porous PDMS has been used in a number of applications such as selective oil absorption [57], storing and releasing aqueous solutions [58], oil-water separation [59] etc. Additionally, porous PDMS collapses easily during compression due to the low mechanical strength of its flexible beam-like structure [57], making the middle layer of SMµRs an excellent drug storage and drug release medium.

Here, I propose to fabricate SMµRs as a multilayer elastomeric composite comprising three layers: the top and bottom layers are made of Polydimethylsiloxane (PDMS) with embedded magnetic micro-particles aligned along the length or the width of the SMµRs. The middle layer is made of porous PDMS, which act as a reservoir for drugs and liquid biopsies. Nanopatterns on the top and bottom surfaces of the SMµRs increase their traction with the environment during locomotion.

2.2 Fabrication of SMµRs

Fabrication of the bottom layer of the SMµRs: I used PDMS (SYLGARD 184) and magnetic powder (Neodymium Iron Boron—NdFeB—alloy powder, particle size 150 µm, 99% purity) as the base materials for fabricating the top and bottom layer of SMµRs. To begin the process, I mixed PDMS elastomer with its corresponding platinum-based curing agent in a 10:1 ratio. After I thoroughly mixed PDMS prepolymer for a minimum of two minutes, I added 5 g of magnetic powder to the mixture to have 1:1 ratio (mass of PDMS to the mass of magnetic powder).

I also added 0.5 g of caster sugar to the mixture to create the porous middle layer of the SMμRs by templating the sugar and removing it by dissolution in warm water (Figure 2.2a). After stirring the mixture by hand for a minimum of five minutes, I placed the mixture inside a desiccator at 36 Torr for 5 mins to remove the air bubbles.

Note on materials and fabrication approaches: Initially, I used iron powder to actuate SMμRs, but it was not possible to induce enough magnetization for inducing the desired tumbling locomotion. This is the reason why I used magnetic powder. Ecoflex 00-30 Platinum cure silicone rubber (Smooth-on, Inc.) was used first as the base material to fabricate SMμRs. The high elasticity of Ecoflex and its sticky surface enabled the magnetic particles to rotate within the polymer even after curing. Consequently, I could not get the desired alignment of the magnetic micro-particles to achieve tumbling locomotion.

2.2.1 Enhancing the Traction of the Microrobots Adding Nanopatterns to their Surface

Nanotexturing the surfaces of the SMμRs enhances the traction of the microrobots with the surfaces they are in contact during locomotion [60]. I used soft lithography principles to fabricate nanopatterns *via* replica molding using polymeric gratings (Figure 2.1a). Polymeric gratings were obtained from compact disc (CDs; Sony Corp., USA). I removed the top labeling layer of the CD using packaging tape (3M Inc.). The reflective ink coating of the CD micropatterns (periodic grating) was dissolved and washed away using isopropanol (IPA). After drying the grating with a stream of nitrogen for ~1 min, I carefully spread the mixture of PDMS prepolymer, magnetic powder, and caster sugar on the polymeric grating (Figure 2.2b).

2.2.2 Alignment of Magnetic Particles in a Polymeric Matrix Using Global Fields

To achieve tumbling lengthwise and sidewise locomotion and being able to release the content of the microrobots at targeted areas, I aligned the magnetic micro-particles inside the mixture along the length for lengthwise locomotion and along the width for sidewise locomotion. I placed the polymeric grating over a strong NdFeB permanent magnet for 5–10 mins to align the magnetic particles inside the mixture (Figure 2.1b, 2.2c). I then placed the mixture inside an oven at 60 °C for 2 h to cure the mixture completely. After curing, I put the polymeric grating into a glass beaker and covered it with warm water and sonicated it to dissolve the sugar particles. 1 h of sonication

dissolved all the sugar particles within the composite (Figure 2.1c). After drying the composite using dry nitrogen, the fabrication of the bottom layer of SMμR containing aligned magnetic micro-particles embedded in it and the middle porous PDMS layer (Figure 2.2d) was complete. At this state, drugs can be deposited inside the porous layer prior to their final encapsulation with the top layer of the SMμR. I used blue food coloring dye to simulate a drug. I put the dye inside the porous layer and kept it inside a desiccator for 2 mins so that the dye could be fully absorbed by the porous PDMS (Figure 2.1d).

Fabrication of the top layer of the SMμRs: I followed the same procedure described above to fabricate the top layer of SMμRs, without adding sugar to the mixture of PDMS and magnetic powder. Since no sugar was used in the fabrication of the top layer of SMμRs, it does not contain any pores. I used a razor blade to remove the top and bottom layers from the polymeric grating (Figure 2.1e). Finally, I assembled top, middle, and bottom layers of the SMμRs, using PDMS prepolymer and cured the ensemble at 60 °C for 2 h (Figure 2.1f).

2.2.3 Laser Micromachining of SMμRs

I used a laser engraving system (#3802; LaserStar Inc.) to cut the desired size of the SMμRs (three cutting cycles to reduce over heating; laser power = 50 W; speed = 500 nm min^{-1}). The dimensions of the fabricated SMμRs are, approximately, length, L = 750 μm; width, W = 500 μm.

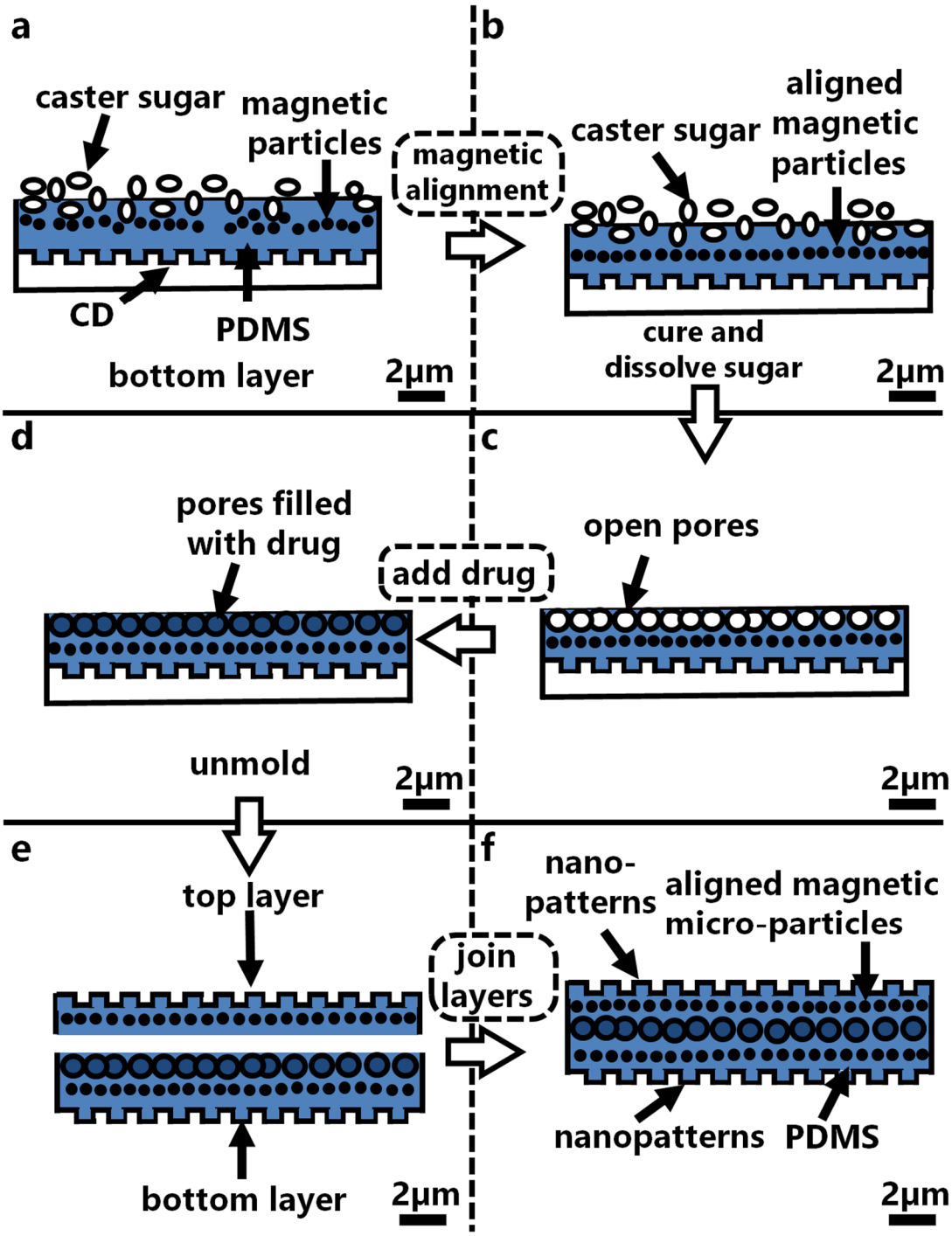

Figure 2.1. Schematic diagram of the fabrication process of SMμRs. (a) A mixture of PDMS, magnetic powder, and caster sugar is deposited on top of a polymeric grating. This grating will enhance the traction of the microrobots. (b) The mixture is kept over a magnet to align the magnetic particles along a preferential direction. (c) The mixture is cured and then sonicated to dissolve the sugar particles to create pores in its structure. (d) The open pores are filled with drug. I used blue dye to simulate drug. (e) The two layers are unmolded from polymeric grating. (f) The top layer is attached to the middle and bottom layers to get SMμRs.

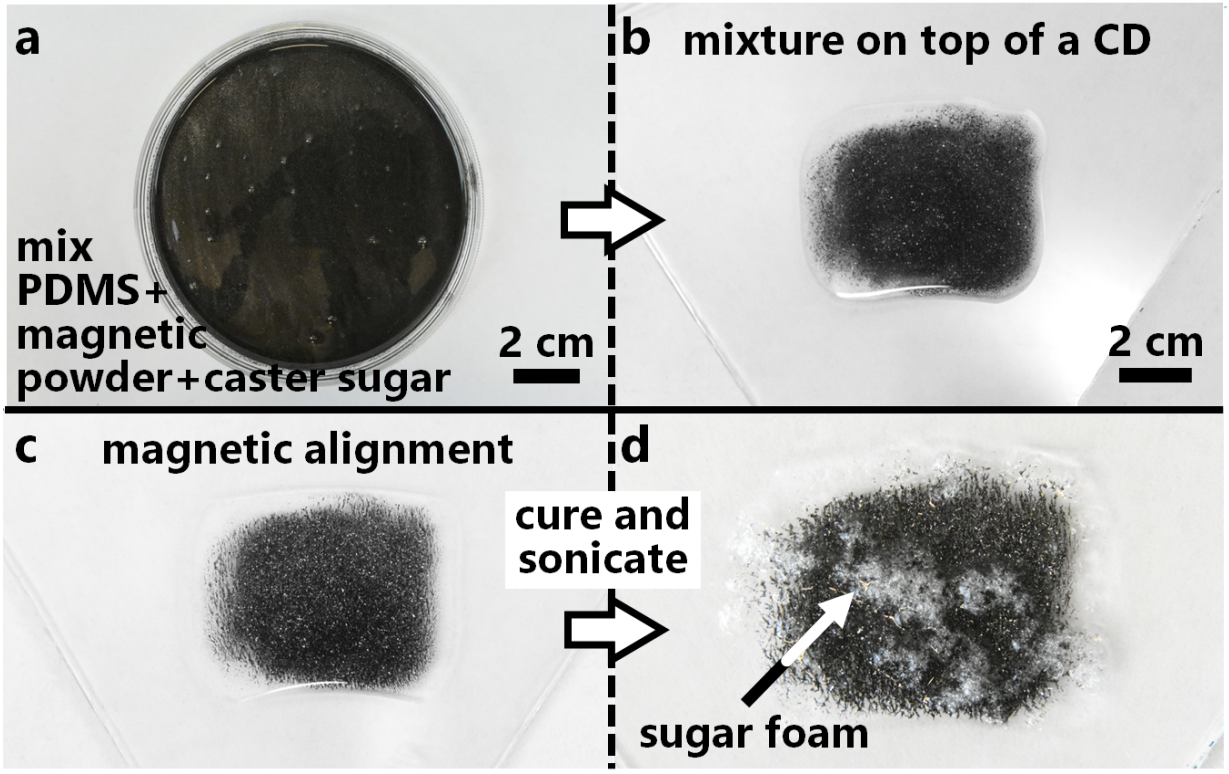

Figure 2.2. Step-by-step fabrication of SMµRs. (a) PDMS, magnetic powder, and caster sugar are mixed together. (b) The mixture is spread over a polymeric grating to incorporate nanopatterns. (c) The polymeric grating is then placed over a permanent magnet to align the magnetic particles inside the mixture. (d) The mixture is cured and then sonicated to dissolve sugar particles.

2.3 Biocompatibility of the SMµRs

PDMS is a biocompatible elastomer [61]. When I put the mixture of PDMS and magnetic micro-particles on top of the polymeric grating, as the grooves in the polymeric grating are smaller (~800 nm) than the average size of the magnetic micro-particles (~150 µm), only PDMS gets into the grooves of the gratings. Moreover, since the magnetic particles are heavier than PDMS, they accumulate at the bottom (on top of the polymeric grating), leaving a layer of PDMS on top when the mixture was cured. In other words, PDMS encapsulates all the magnetic micro-particles impeding their accidental release. Therefore, the top and bottom surfaces of the SMµRs are biocompatible (PDMS) and the porous structure inside the SMµRs is hydrophobic which impedes the diffusion of the internal payload while tumbling over mucosa-coated tissues.

2.4 Scanning Electron Imaging

I used a scanning electron microscope (Nova NanoSEM200, FEI, Hillsboro, OR, USA) to examine the structure of caster sugar particles (Figure 2.4a), magnetic particles (Figure 2.4b), and to examine the nanopatterns on the surfaces of fabricated SMμRs (Figure 2.3). Before imaging, I used a sputter coater (208HR, Cressington, UK) to create a uniform conductive coating of ~10 nm platinum, using a D.C. current of 40 mA for 60 s. SEM images of the samples were captured at an electron accelerating potential of 5kV, spot size 3, and working distances of between 3-5 mm using an Everhart-Thornley detector (ETD).

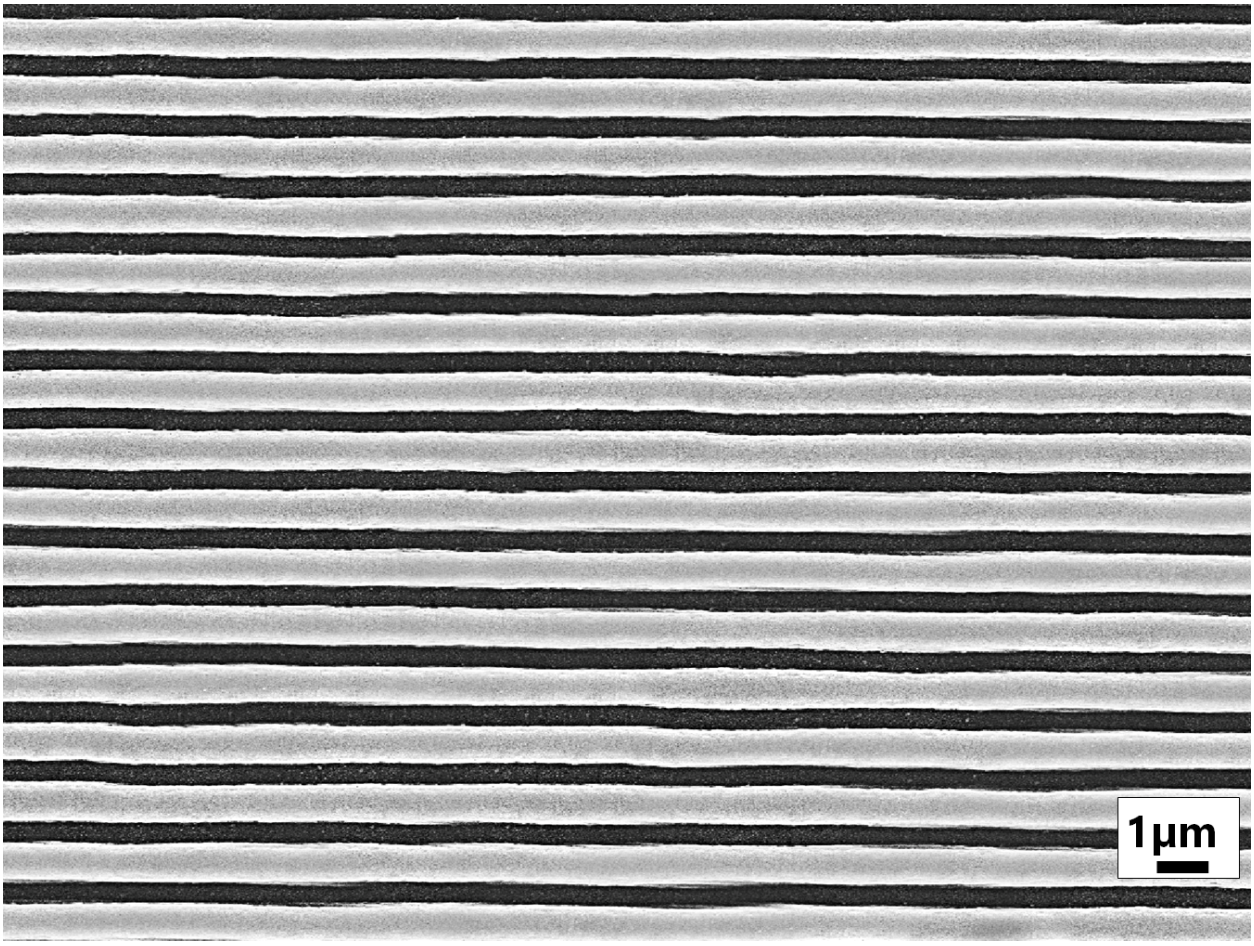

Figure 2.3. SEM image of polymeric grating. The pitch of the polymeric grating is 1.6 μm.

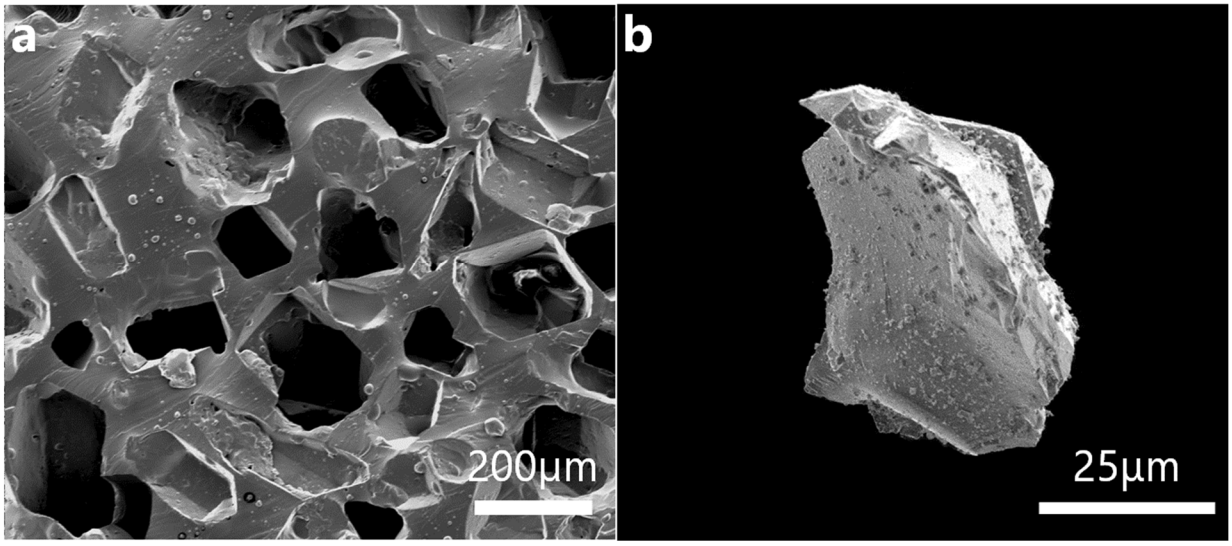

Figure 2.4. (a) SEM image of porous PDMS based on caster sugar template. (b) SEM image of a magnetic particle. The average diameter of the magnetic particles is 150 µm.

2.5 Cost of Fabrication

I estimate the cost of fabricating each SMµR (L = 750 µm; W = 500 µm) to be less than $0.07. This total cost, itemized in table, is based on costs of small amount of the materials used for the fabrication and can be minimized for larger production.

Table 2.1. Itemized cost of materials to fabricate a SMµR.

Cost of SMµR	
Magnetic powder	$0.048
PDMS	$0.01
Polymeric grating (re-usable)	$0.001
Caster sugar	$0.001
Total cost	**$0.06**

3. WIRELESS CONTROL OF SMµRs USING ROTATING MAGNETIC FIELDS

3.1 Inducing Tumbling Motion Using Rotating Magnetic Fields

Many magnetically controllable microparticles and microrobots are dragged over surfaces using continuous external magnetic fields. This actuation mechanism often fails to power those microparticles or microrobots that become stuck in an obstacle. Recently, to overcome this limitation, continuously rotating magnetic fields have been used to exert a continuous torque on microrobots, inducing their tumbling motion to align with the external field [48]. Such controllable tumbling locomotion facilitates the overcoming of obstacles to microrobots.

To control the magnitude and direction of the rotating magnetic fields, I used a magnetic actuation setup comprising NdFeB disk magnets (32 mm diameter × 2 mm thickness) which were mounted on the shaft of a DC gear motor (Figure 3.1b). The rotational frequency of the magnet can be controlled by varying the voltage applied to the DC motor. The rotational frequency of the actuating magnet can be calculated in rev/min using the following formula:

$$f = \frac{(n \times 60)}{t} \text{ rev/min}$$

where, f = rotational frequency of the magnet; n = no. of rotations; t = time in seconds needed to complete the rotations.

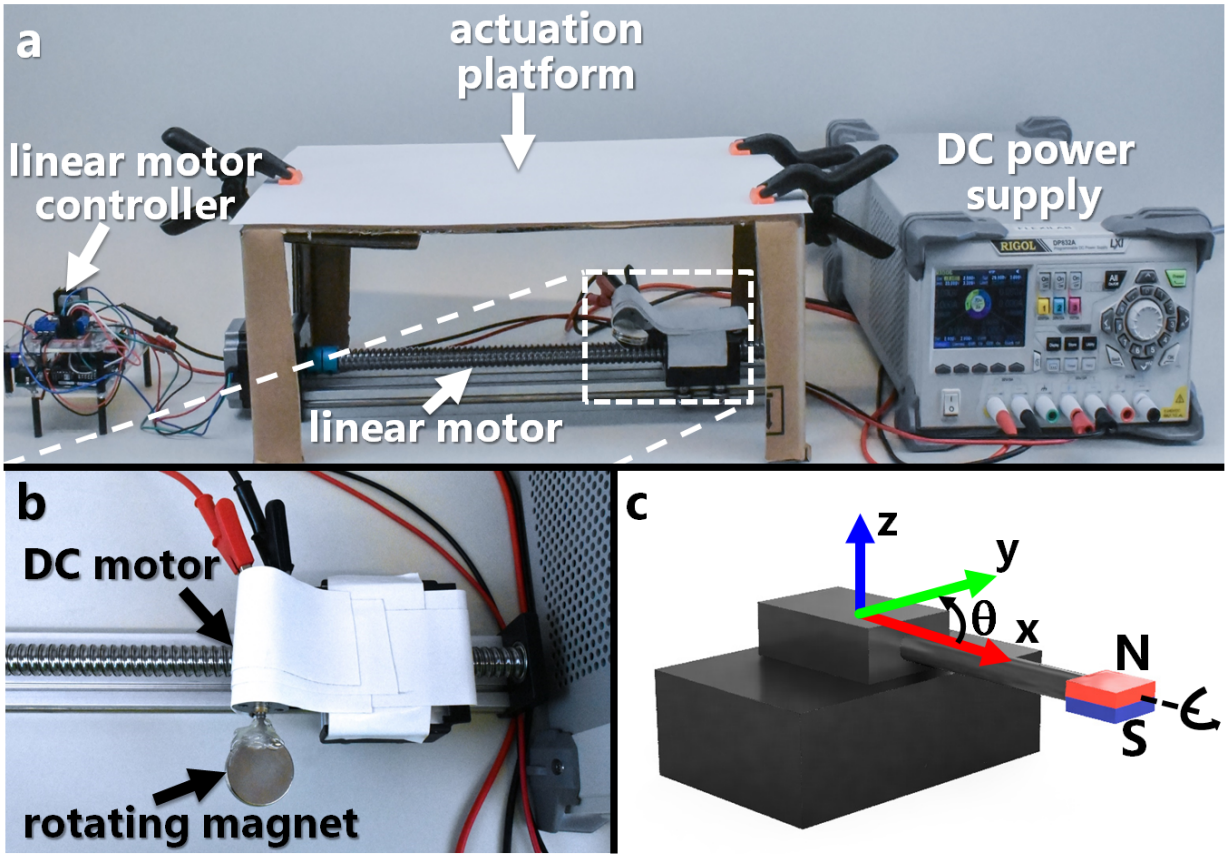

Figure 3.1. (a) Photograph of the experimental setup used to actuate SMµRs. (b) Zoom-in showing the actuating magnet attached to the end of a DC motor shaft (underneath the white tape). (c) Schematic representation of the movable magnetic stage used to actuate SMµR *via* rotating magnetic fields.

To control the position of the rotating magnet, I mounted the DC motor on a stage attached to a linear motor (Figure 3.1a). I placed the SMµRs on the actuation platform at a distance of 60 mm above the rotating permanent magnets, since I experimentally found that the distance between the actuating magnet and the SMµR needs to be smaller than 65 mm to induce tumbling locomotion. For these particular magnets, the separation from the SMµRs needs to be between 40–65 mm for their appropriate actuation. How the magnetic field intensity changes with distance for this magnet can be found in Figure 4.2. With the increase of the strength of the actuating magnetic field, the distance between the SMµRs and the actuating magnets can be increased. The rotating permanent magnet wirelessly generates torque on the SMµRs. As a result, the SMµRs tumble sidewise or lengthwise depending on the alignment of magnetic particles. I calculated the speed of the SMµRs

by measuring the distance travelled by the SMµRs and the time required to travel that distance at different rotational frequencies. At least five speed values will be used to obtain an average and associate that speed to the shape and magnetization of the SMµR and the viscosity of the surrounding media (Figure 4.1). The average speed of the SMµR depends on its size and is proportional to the rotational frequency of the actuating permanent magnet.

3.2 Measurement of the Magnetic Field Intensity

To quantify the intensity of the rotating magnetic fields used to control the motion of the SMµRs, I used a Hall effect sensor (Model: GY-9250 MPU9250, UCTRONICS Inc.). Measurements from this sensor are collected using a portable microcontroller (Arduino UNO, ARDUINO Inc.). To interface with the Hall sensor, I used I2C communication with sampling rate of 100 Hz. The Arduino code written to collect the readout of the sensor after averaging 200 consecutive values can be found in the Appendix (Code A1).

To calibrate the sensor, I assigned to the ambient field measurement a reference value of 0 T in all the three axes (Figure 3.2c). I used a "calibration coil" to create a known field in all the three axes, separately. I calculated the known field mathematically by using the equation of magnetic field of a current carrying loop:

$$B_z = \frac{\mu_0}{2} \frac{NR^2 I}{\left(z^2 + R^2\right)^{3/2}}$$

Where, μ_0 = free space permeability= $4\pi \times 10^{-7}$ H/m;

R = radius of the coil = 0.0141 m;

N = number of turns of the coil = 25;

I = current passing through the coil = 1 A;

z = distance from loops along z axis = 11.47 mm.

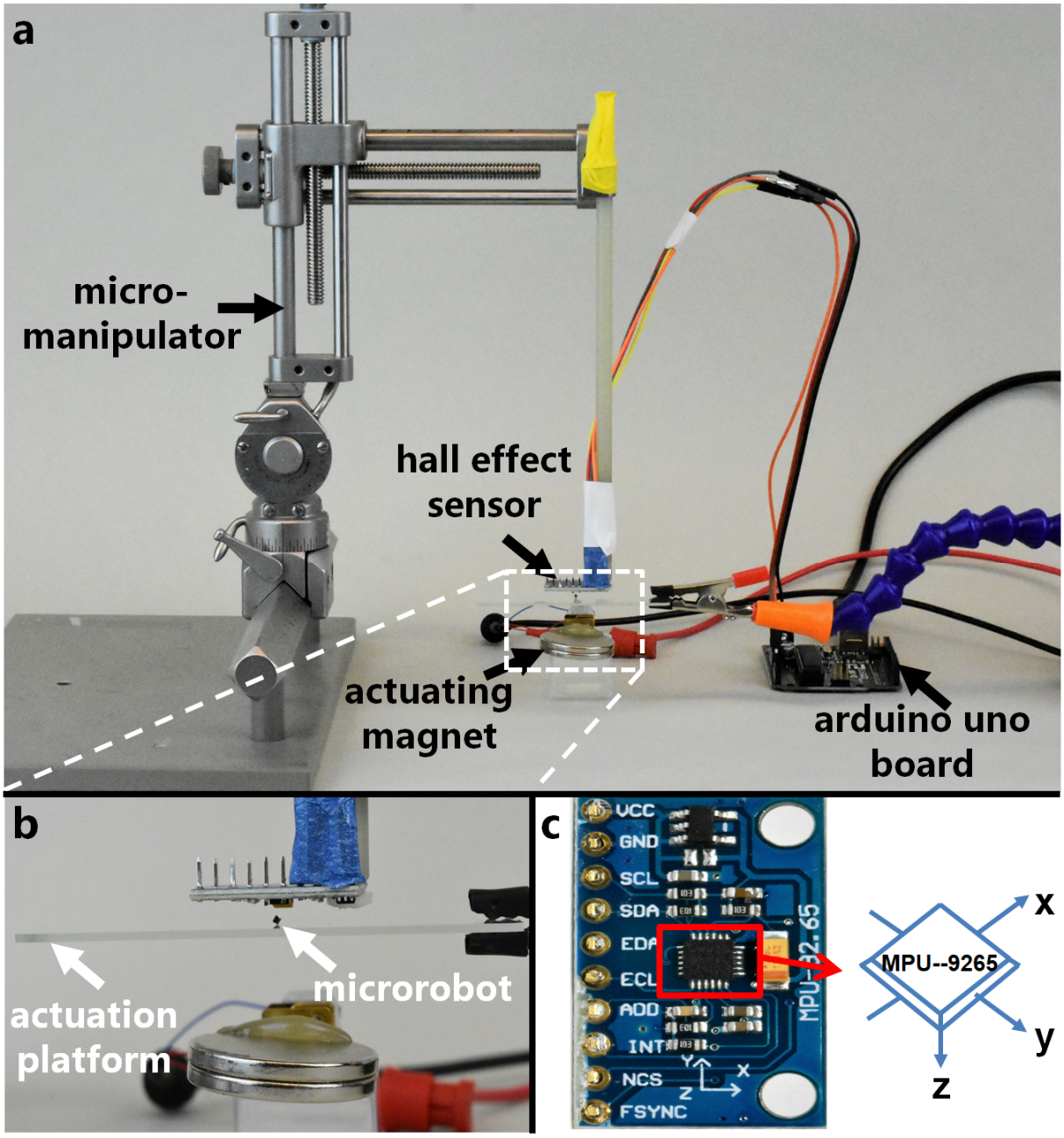

Figure 3.2. (a) Photograph of the experimental setup used to measure the intensity of the magnetic field. (b) Zoom-in showing the actuating magnet, microrobot on the actuation platform and hall effect sensor. (c) Schematic representation of the orientation of the axes of hall effect sensor.

Using the theoretical value of the magnetic field, I calibrated the readouts of the sensor along its three axes. I attached the magnetic field sensor to a non-magnetic rod connected to a micromanipulator (Figure 3.2a). I measured the magnetic field by varying the distance between

the actuating magnet and the SMµRs to get the variation of magnetic field intensity with distance (Figure 3.2b). Accuracy is very high for the positions since the micromanipulator is very precise.

3.3 Controlling the Tumbling Motion of SMµRs

Tumbling locomotion enables the SMµRs to pass through unknown and difficult to reach locations overcoming obstacles [48]. Depending on the direction of alignment of the magnetic particles inside the SMµR (along its length or along its width), I can achieve two types of tumbling locomotion: lengthwise and sidewise, respectively. If the direction of alignment of the magnetic particles inside SMµRs is different from the external magnetic field direction, it induces a magnetic torque on the SMµR, which tumbles to realign the magnetic particles embedded in its porous structure with the external field. The continuous rotation of the magnetic field results on the periodic tumbling of the microrobots in the direction of rotation of the magnet, achieving tumbling locomotion. To achieve sidewise and lengthwise tumbling locomotion—tumbling of the microrobot along its width and length—I used a vertically rotating external field (along z-axis; Figure 3.3a, 3.4a). Moreover, depending on the direction of the external magnetic field rotation (clockwise or anti-clockwise), SMµRs can move along forward or backward direction.

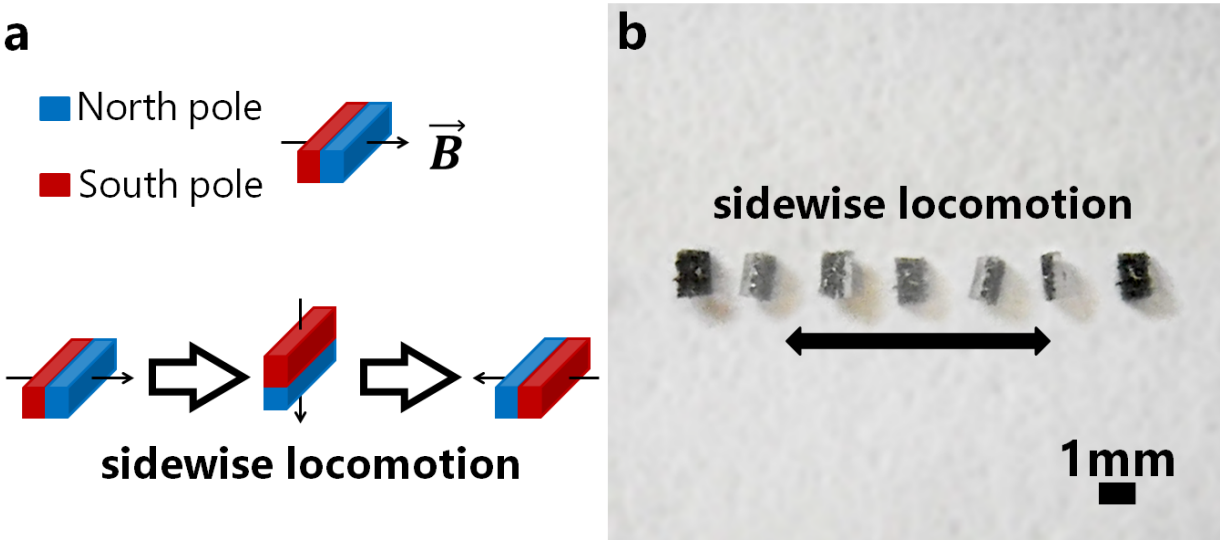

Figure 3.3. Sidewise tumbling locomotion of SMµR. (a) Schematic diagram of the structure of a SMµR capable of sidewise translation. (b) Superimposed frames showing the forward and backwards sidewise locomotion of a SMµR.

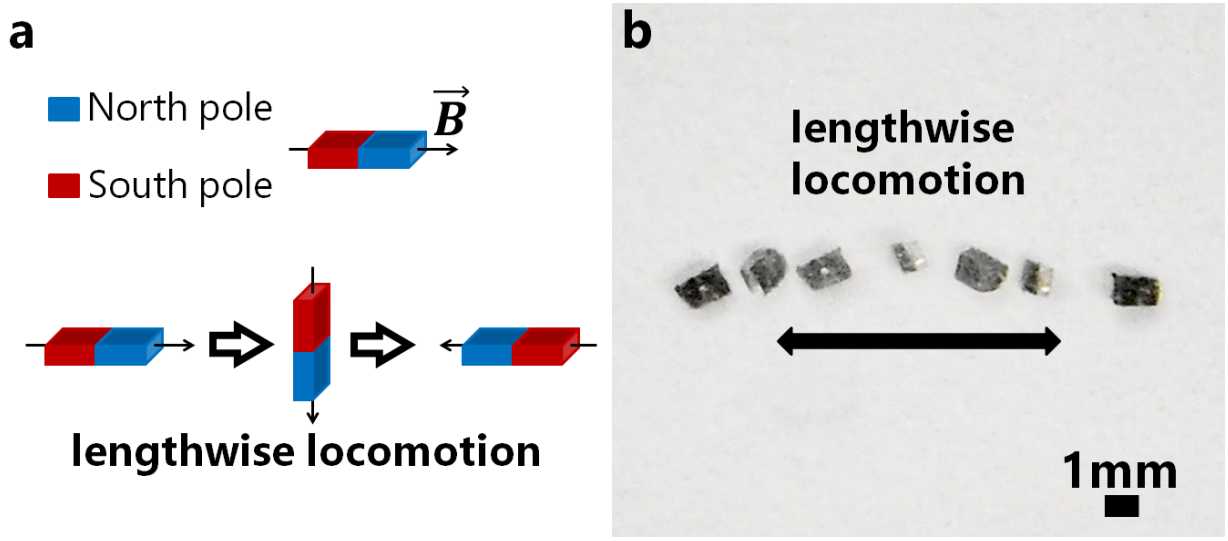

Figure 3.4. Lengthwise tumbling locomotion of SMµR. (a) Schematic diagram of the structure of a SMµR capable of lengthwise translation. (b) Superimposed frames showing the forward and backwards lengthwise locomotion of a SMµR.

Figure 3.3b and 3.4b show the sidewise and lengthwise tumbling locomotion of SMµRs, in forward and backward direction, respectively. SMµRs can also follow a particular trajectory. To demonstrate this, I made a SMµR follow a square-like trajectory (Figure 3.5). Sidewise locomotion has two main advantages when compared with lengthwise locomotion: i) It requires less magnetic force to tumble the microrobot. ii) The smaller amplitude of the tumbling motion makes the microrobot less affected by dragging forces [48]. I therefore used sidewise tumbling as the primary tumbling mechanism to move SMµRs.

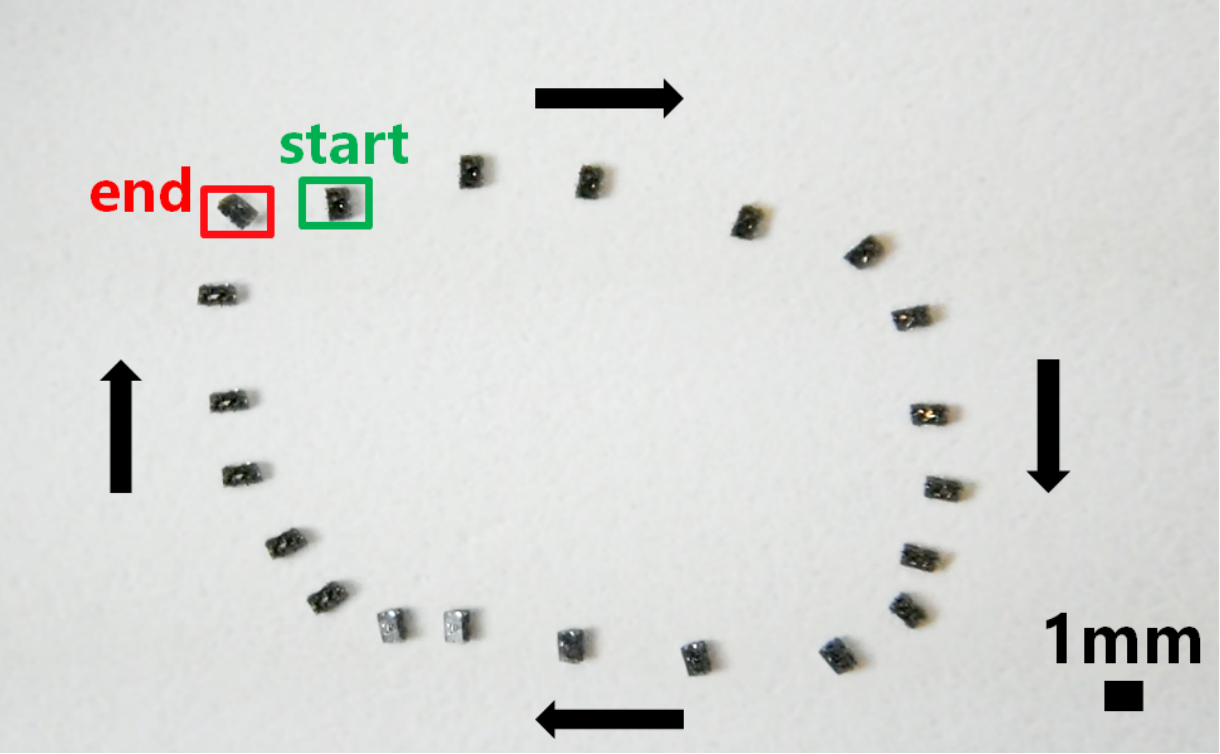

Figure 3.5. Superimposed frames showing the capability of SMμRs to follow a square-like path.

3.3.1 Kinematic Analysis

I computed the trajectory and speed of the microrobots for each locomotion modality by tracking the position of the centroid of the microrobot. I used the Image Processing ToolboxTM available in MATLAB 2016a (Mathworks Inc.) to analyze orthographic videos (top view) recorded at 30 frames per second at a resolution of 1920 × 1080 pixels (Appendix, Code A2). For each frame, I first converted it to grayscale and then binarized the image using a thresholding algorithm controlled by a set-level parameter. These operations make the background completely white and the microrobot completely black, improving the accuracy of the tracking algorithm. I then calculated the centroid of all the black pixels and plotted the x and y positions of the centroid as a function of time. The instantaneous speed was calculated as the time-derivative of the position (Figure 3.6).

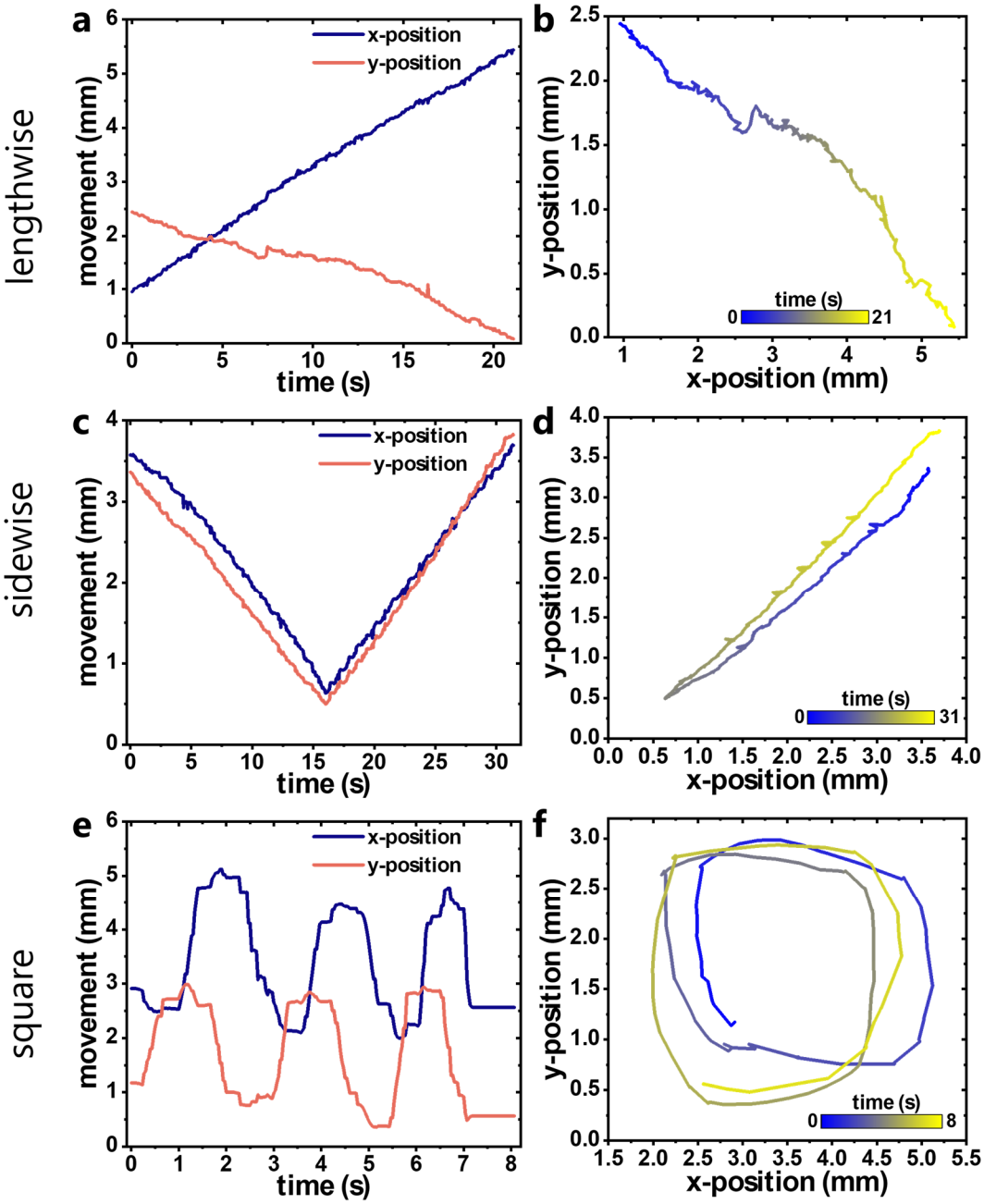

Figure 3.6. Kinematic analysis of a magnetic microrobot. I used MATLAB 2016a (Mathworks Inc.) Image Processing Toolbox™ to track the position of the center of mass (centroid) of the magnetic microrobot.

3.4 Tumbling Locomotion in Obstacle-filled Environments

The nanopatterns on both sides of the SMμRs enhance their traction with the surfaces they contact, enabling their motion over highly corrugated and uneven environments. To demonstrate

the capability of SMµRs to move through complex paths filled with obstacles, I 3D printed a maze with different M6 threads engraved on its surface and directed the motion of the SMµRs from the beginning to the end of the maze (Figure 3.7)

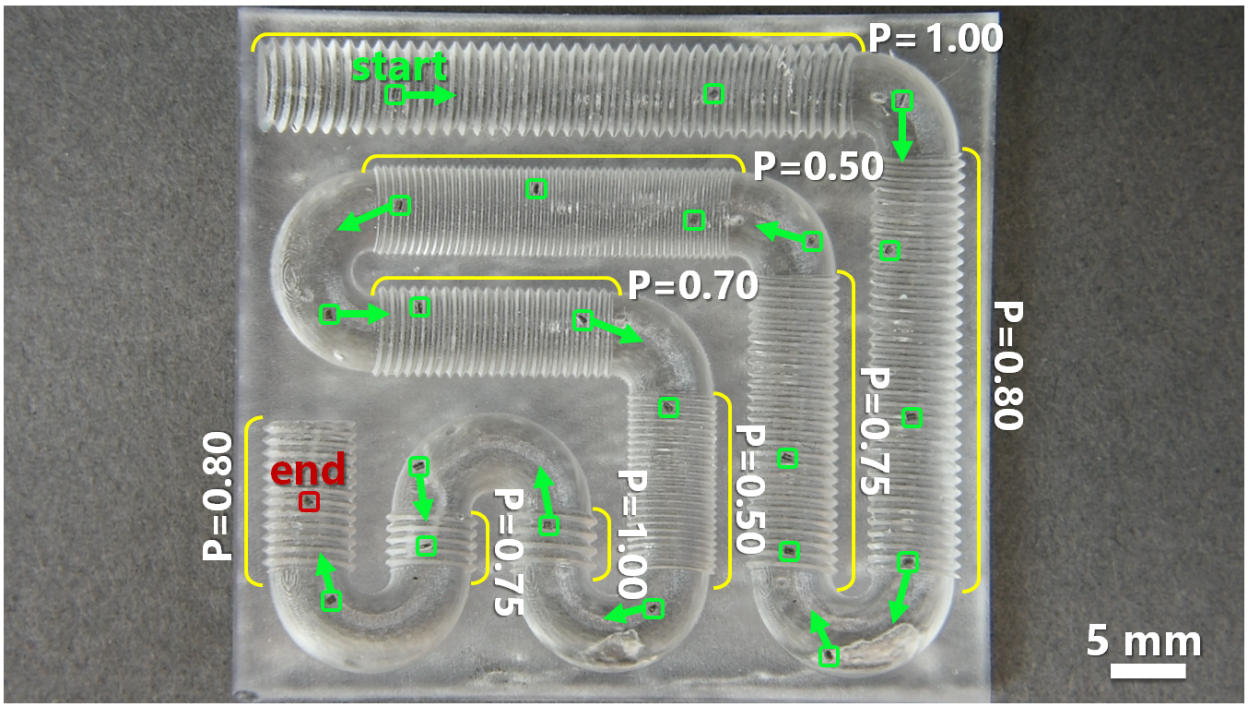

Figure 3.7. Superimposed frames showing the navigation of a SMµR through a 3D printed maze with obstacles of different sizes and pitches.

Figure 3.8a shows the five different pitches of the M6 threads along the maze (1, 0.80, 0.75, 0.70, 0.50). I experimentally found that the average speed of the SMµRs is inversely proportional to the pitch of the thread (Figure 3.8b). This is due to the fact that the height of the obstacle decreases with the pitch, facilitating the SMµR to move through this obstacle quicker for a given rotational frequency of the actuating magnet. I also experimentally found that the average speed of the SMµRs on complex surfaces (such as the maze in Figure 3.7) is lower than that on flat surfaces since the corrugations on these complex surfaces hinder the locomotion of the SMµRs.

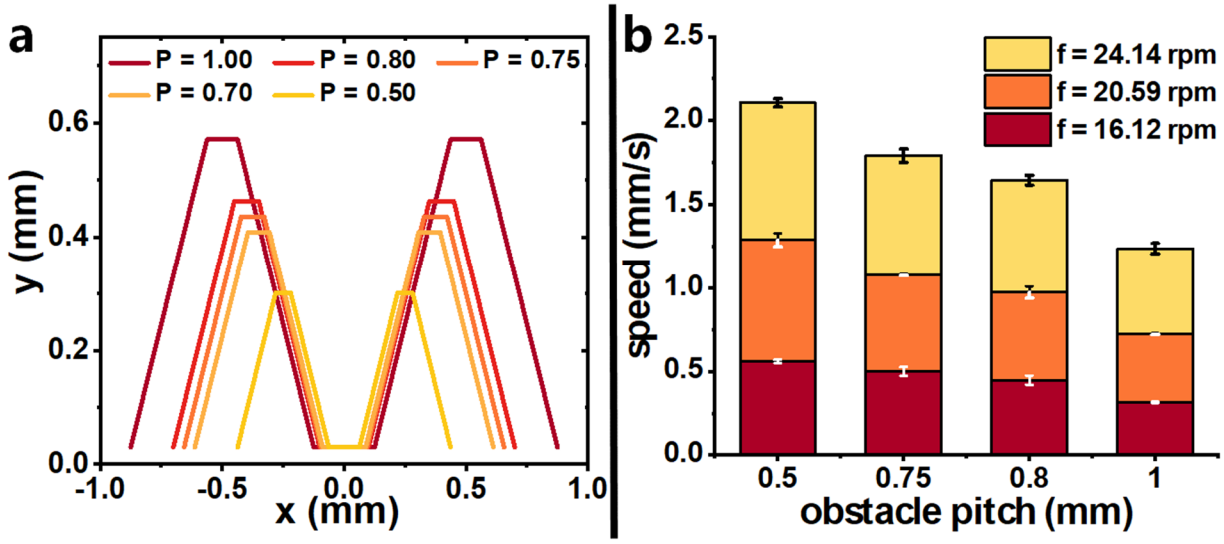

Figure 3.8. (a) Profile of the obstacle threads perpendicular to the direction of the maze. (b) Dependence of the average speed of the SMµRs on the obstacle size and pitch, for different rotational frequencies of the actuating magnetic field.

4. TARGETED DRUG RELEASE USING SMµRS

4.1 SMµR Navigation in Liquid Media

The average speed of the SMµRs varies under different rotational frequencies of the magnetic field for various environmental conditions (Figure 4.1). I experimentally found that the average speed of the SMµRs in air (viscosity ~0.018 cP) increases almost linearly as the rotational frequency of the external field increases up to a certain frequency (350.7 rpm) and then it starts to decrease. In air, I measured a maximum average speed of 24.73 mm/s at a rotational frequency of 350.7 rpm, when the magnetic force tumbling the microrobot is equal to the drag force exerted by the air on the microrobot. Beyond this frequency (>350.7 rpm), the average speed of SMµRs starts to decrease since the coupling between the SMµR and the rotating magnet is lost. Under water (viscosity ~1 cP) buoyant forces decrease the traction of the microrobot on the surface it moves on. The viscosity of water causes the average speed of the SMµRs to saturate at a speed of 17.4 mm/s at a rotational frequency of 393.2 rpm. When immersed in vegetable oil (viscosity ~54.3 cP), its larger viscosity causes the SMµRs not to be able to move forward at frequencies higher than 350.7 rpm. As a result of the lack of coupling between the rotating magnet and the microrobot, SMµRs oscillate in the same place instead of moving forward. Due to its higher viscosity, the average speed in vegetable oil is lower than that in air and water. I measured the maximum average speed of 9.77 mm/s in vegetable at 310.5 rpm.

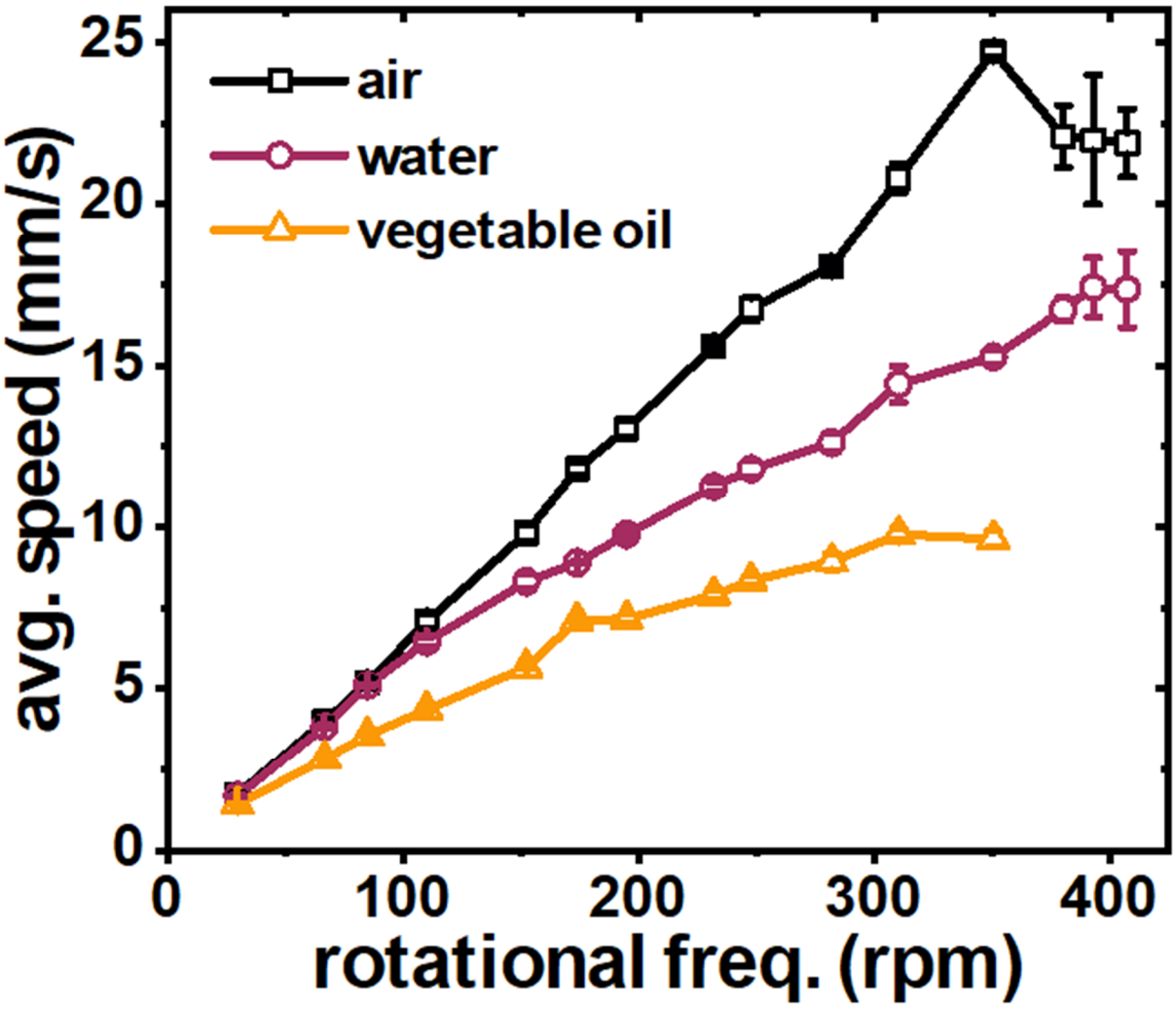

Figure 4.1. Dependence of the locomotion speed of the SMμR in different media (air, water, and vegetable oil) on the rotational frequency of the actuating magnet.

4.1.1 Dependence of the Magnetic Field Intensity on the Distance between Magnet and SMμR

Figure 4.2 shows how the magnitude of magnetic field intensity |B| changes as a function of distance for the magnet that I used in the experiment. I calculated the theoretical magnetic field intensity using the following formula:

$$\boldsymbol{B} = \frac{B_r}{2}\left(\frac{D+z}{\sqrt{R^2+(D+z)^2}} - \frac{z}{\sqrt{R^2+z^2}}\right)$$

where, B_r = remanence field; z = distance from a pole face on z axis; D = thickness of the magnet= 2 mm; R = radius of the magnet = 16 mm.

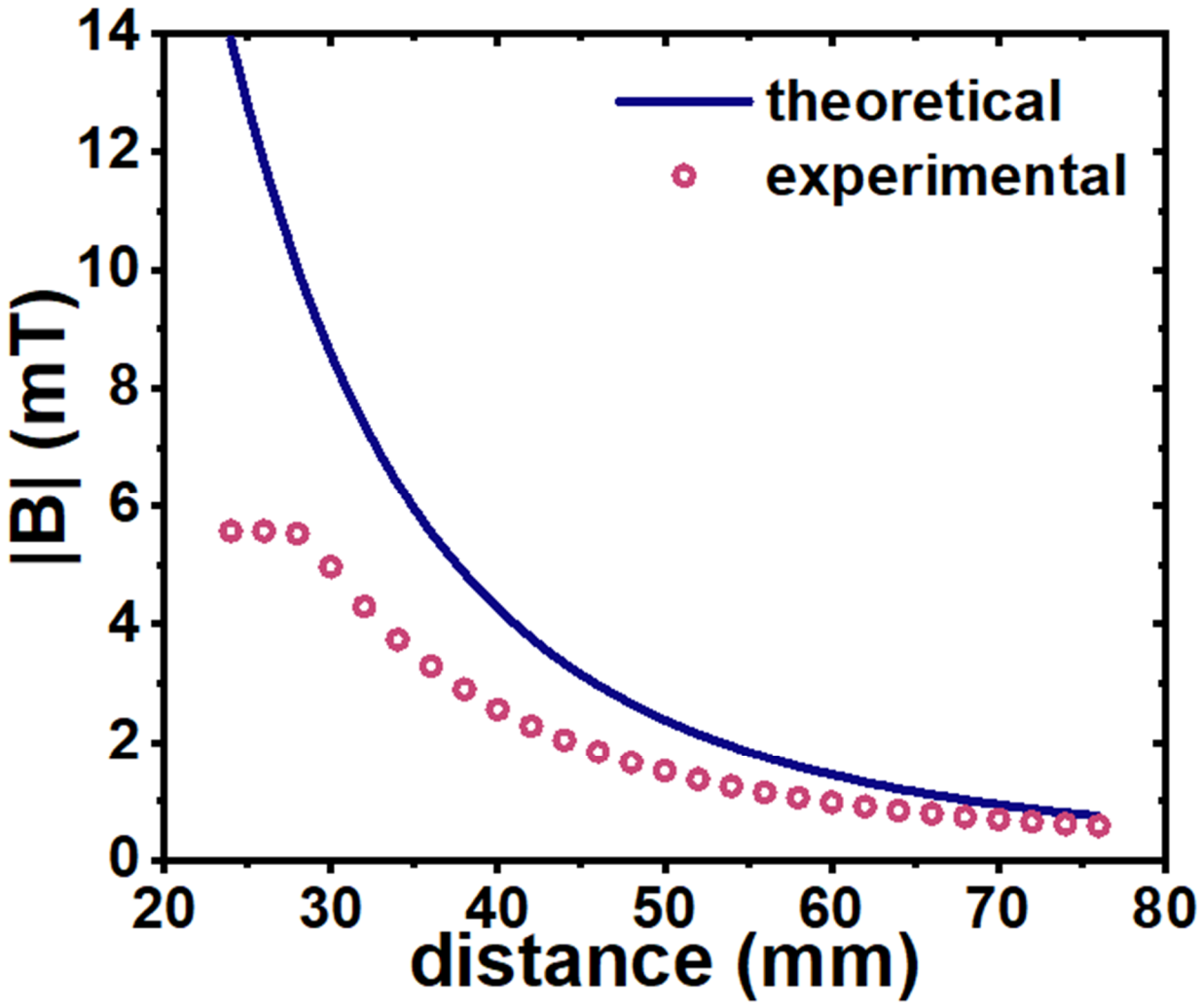

Figure 4.2. Variation of the magnitude of magnetic field intensity, |B|, along the axis perpendicular to the surface of the rotating magnet as a function of the distance to the magnet.

I then compared the experimental magnetic field intensity with the theoretical one and found that the theoretical and experimental results match within experimental limits. In experiment, the value saturated at 5.6 mT as the sensor I used cannot measure magnetic field intensity more than 5.6 mT along z axis. Using this graph, I calculated the magnetic field intensity needed to induce tumbling and to release the drug by knowing the distance between the SMμR and the magnet.

4.1.2 Collapsing the Porous Layer of SMµRs Using Extended Magnetic Fields

I experimentally calculated the magnetic field intensity needed to collapse the porous structure of the middle layer of the SMµRs to be able to remotely control their drug release. Figure 4.3 shows how, *in vitro*, when the targeted location was reached, I increased the magnetic field intensity by decreasing the distance between actuating magnet and the SMµR, which collapsed the porous structure of the microrobot and liberated its drug content.

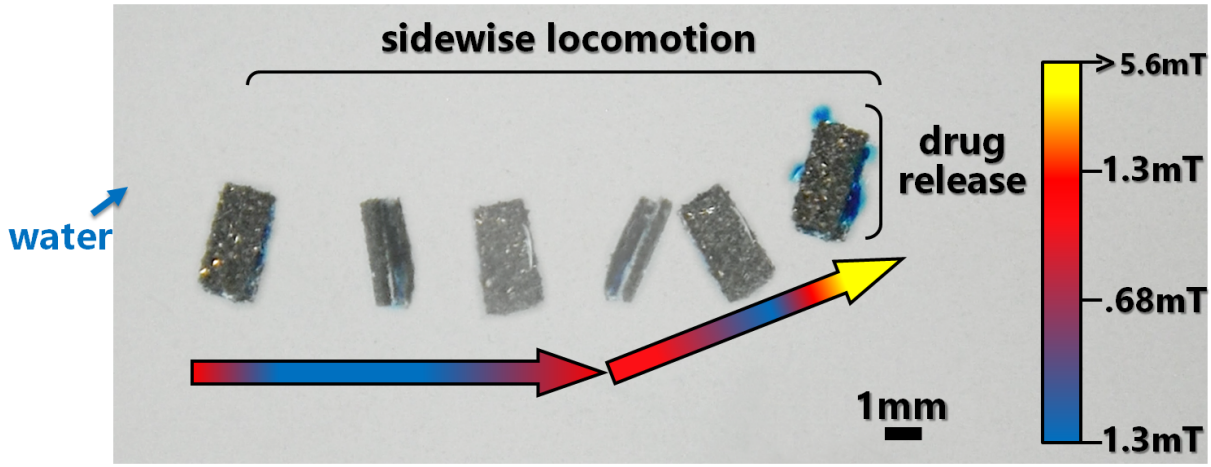

Figure 4.3. Superimposed frames showing the sidewise locomotion and targeted drug delivery of SMµR in water. Colored arrows represent the direction and the module of the magnetic field.

4.2 Discrete and Continuous Drug Delivery Along Gastrointestinal Tissue

Tumbling locomotion enables the drug loaded SMµRs to navigate through the gastrointestinal tract overcoming the obstacles that the mucosa and the corrugated walls of the intestine cause to conventional microrobots or magnetic nanoparticles. To demonstrate this, I took a section of pork intestine which represents a rough, soft, biologically relevant surface for the SMµRs. Then, I put the intestine inside a petri dish with the inner surface facing up. Figure 4.4 shows the combined sidewise locomotion of SMµRs over the surface of the gastrointestinal tissue and the controllable discrete and continuous drug release at specific locations of the tissue.

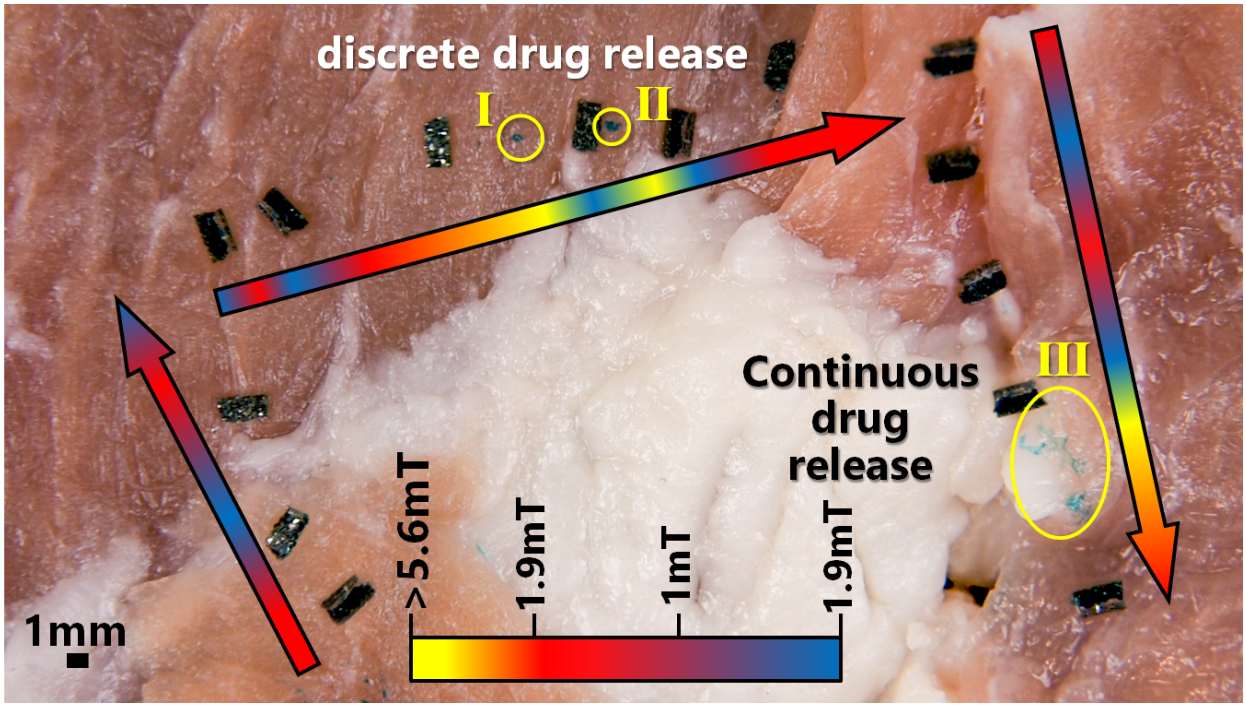

Figure 4.4. Superimposed frames showing the navigation of the SMµR (in the direction of the arrows) and the discrete and continuous drug delivery over gastrointestinal tissue using a SMµR. The color of the arrows represents the direction and the module of the magnetic field along the path of the SMµR.

Figure 4.5a shows the topological reconstruction of the gastrointestinal tissue used for the experiment. Discrete drug release was done by pausing the tumbling locomotion while continuous drug release was done without pausing (Figure 4.5b). In vivo, there is a mucus layer on gastrointestinal tract which protects the GI tract from bacterial attack [3]. The presence of this viscous layer might limit the locomotion of nanoscale tumblers. I demonstrated that the presence of nanopatterns on surfaces of the SMµRs enables them to move through viscous media without slipping (Figure 4.1). I therefore expect the mucus layer not to impede the tumbling locomotion of the SMµRs along the GI tract.

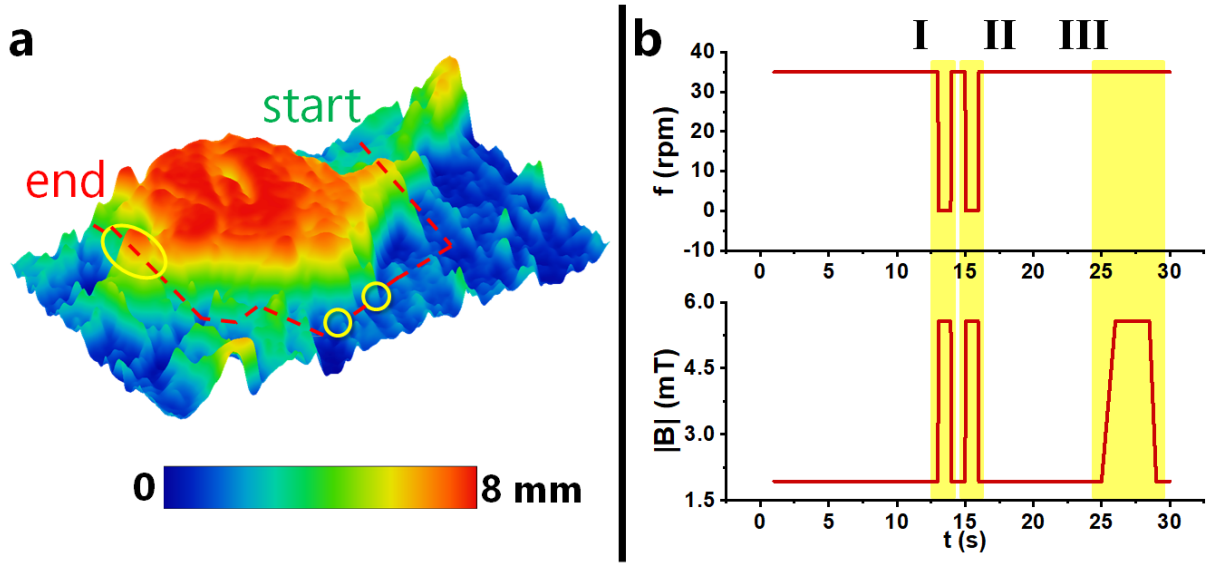

Figure 4.5. (a) Topological reconstruction of the path of the SMμR along the gastrointestinal tissue shown in figure 4.4. (b) Intensity and rotational frequency of the magnetic field applied to translate and release the drug on the areas of the tissue marked in figure 4.4.

5. CONCLUSIONS AND FUTURE WORK

In summary, this work demonstrates a low-cost method to fabricate soft magnetic micro robots and proposes a simple magnetic actuation method to control their tumbling locomotion and drug release. SMµRs fabricated and actuated by this method are soft, lightweight, and have the capability to effectively navigate along flat, corrugated, and unstructured surfaces both forward and backwards, overcoming obstacles in different environmental fluid conditions. Moreover, SMµRs can transport and release drugs to specific locations. SMµRs, at their present level of development have two limitations: (1) It is difficult to control the amount of drug delivered. (2) It is difficult to track the position of SMµRs while inside the body. The fabrication strategy to make the SMµRs is, however, versatile and can be extended to large scale fabrication for potential low-cost medical use.

Future work will focus on using an electromagnetic coil setup instead of permanent magnets to have precise control on SMµRs and to provide higher magnetic field intensity in all directions. Smaller magnetic particles can be used to increase the efficiency of the SMµRs. The SMµRs developed presently can release drug in wet medium as we have used dye as the drug. Other kinds of payloads such as liquid drugs can be incorporated to the SMµRs to use them as minimally invasive, targeted drug release devices or samplers for liquid biopsies. Sensing elements such as force measurement sensor can also be incorporated on board to use the SMµRs for remote sensing applications [25]. SMµRs could also be used in a swarm to increase the amount of delivered drug. Using an appropriate choice of materials SMµRs can be made bioresorbable, facilitating their adoption to treat human patients. For example, SMµRs can be fabricated with polycaprolactone (PCL), iron powder, and caster sugar. As SMµRs will be bioresorbable, there will be no need to release drug with magnetic field and get the SMµRs out of the body after application. SMµRs will tumble to the specific location of the body and drug will be absorbed after a certain time.

APPENDIX

Code A1: Arduino code for magnetic field measurement

```
#include "MPU9250.h"
#include <Wire.h>

//Initialization
// an MPU9250 object with the MPU-9250 sensor on I2C bus 0 with address 0x68
MPU9250 IMU(Wire,0x68);
int Status;

void setup()
 {
  // serial to display data
  Serial.begin(9600);
  // start communication with IMU
  Status = IMU.begin();
  if (Status < 0)
{
    Serial.println("IMU initialization unsuccessful");
    Serial.println("Check IMU wiring or try cycling power");
    Serial.print("Status: ");
    Serial.println(Status);
    while(1) {}
  }
    if (Status > 0)
 {
    Serial.println("IMU initialization successful");
    Serial.print("Status: ");
    Serial.println(Status);
  }
}
void loop()
 {
  float MagX = 0;
  float MagY = 0;
  float MagZ = 0;
  int count;
  int Status;

  for(count = 0;count < 200; count++)
{
    Status = IMU.readSensor();
    MagX += IMU.getMagX_uT();
    MagY += IMU.getMagY_uT();
    MagZ += IMU.getMagZ_uT();
    delay(10);
    if (Status < 0)
   {
      Serial.println("Something is wrong");
      Serial.print("Status: ");
      Serial.println(Status);
    }
  }

  MagX = MagX/count; //take the average of 200 data points
```

```
  MagY = MagY/count;
  MagZ = MagZ/count;

  Serial.print(MagY,2); //output 2 decimal places
  Serial.print("\t");
  Serial.print(MagX,2);
  Serial.print("\t");
  Serial.println(MagZ,2);
}
```

Code A2: MATLAB code for tracking microrobots

```
v = VideoReader('movieFile.mp4');
frameCount = 1;
tracking = zeros(50,3); %initializing the matrix tracking which will store values of centroid
coordinates for each frame
while hasFrame(v) %for each frame in the video do the following
    video = readFrame(v);
    gray = rgb2gray(video); %convert RGB frame to grayscale
    BW = imbinarize(gray); %convert grayscale frame to binary
    BW = imcomplement(BW); %invert the binary frame (i.e. black region becomes white, and white
becomes black), since regionprops function finds centroid of white region
    stats = regionprops(BW);
    centroid = stats.Centroid;
    tracking(frameCount,:) = [frameCount,centroid];
    frameCount = frameCount+1;
end
%%All functions used above the detailed below:
function BW = imbinarize(I, varargin)
%IMBINARIZE Binarize image by thresholding.
%   BW = IMBINARIZE(I) binarizes image I with a global threshold computed
%   using Otsu's method, which chooses the threshold to minimize the
%   intraclass variance of the thresholded black and white pixels. BW is
%   the output binary image.
%
%   BW = IMBINARIZE(I, METHOD) binarizes image I with the threshold method
%   specified using METHOD. Available methods are (names can be
%   abbreviated):
%
%   'global'    - Global image threshold using Otsu's method, chosen to
%                 minimize the intraclass variance of the thresholded black
%                 and white pixels. See GRAYTHRESH for details.
%
%   'adaptive'  - Locally adaptive image threshold chosen using local
%                 first-order image statistics around each pixel. See
%                 ADAPTTHRESH for details.
%
%   BW = IMBINARIZE(I, 'adaptive', PARAM1,VAL1,PARAM2,VAL2,...) binarizes
%   image I using name-value pairs to control aspects of adaptive
%   thresholding.
%
%   Parameters include:
%
%   'Sensitivity'           - Specifies the sensitivity factor in the range
%                             [0 1] for adaptive thresholding. A high
%                             sensitivity value leads to thresholding more
```

```
%                             pixels as foreground, at the risk of
%                             including some background pixels. Default
%                             value: 0.50
%
%   'ForegroundPolarity'    - Specifies the polarity of the foreground with
%                             respect to the background. Available options
%                             are:
%
%           'bright'        : The foreground is brighter than the
%                             background. (Default)
%           'dark'          : The foreground is darker than the background.
%
%   BW = IMBINARIZE(I, T) binarizes image I using threshold T. T can be a
%   global image threshold, specified as a scalar luminance value or a
%   locally adaptive threshold specified as a matrix of luminance values. T
%   must have values between 0 and 1. If T is a matrix, it must be of the
%   same size as image I.
%
%   Class Support
%   -------------
%   The input image I can be a real, non-sparse, 2-D matrix of one of the
%   following classes: uint8, int8, uint16, int16, uint32, int32, single or
%   double. The output binary image BW is a logical matrix of the same size
%   as I.
%
[I,isNumericThreshold,options] = parseInputs(I,varargin{:});
if isNumericThreshold
    T = options.T;
else
    method = options.Method;

    if strcmp(method,'global')
        T = computeGlobalThreshold(I);
    else
        sensitivity = options.Sensitivity;
        fgPolarity  = options.ForegroundPolarity;
        T = adaptthresh(I,sensitivity,'ForegroundPolarity',fgPolarity);
    end

end
% Binarize image using computed threshold
BW = binarize(I,T);
end

function BW = binarize(I,T)
classrange = getrangefromclass(I);
switch class(I)
    case {'uint8','uint16','uint32'}
        BW = I > T*classrange(2);

    case {'int8','int16','int32'}
        BW = I > classrange(1) + (classrange(2)-classrange(1))*T;

    case {'single','double'}
        BW = I > T;
end
end
function T = computeGlobalThreshold(I)
% Otsu's threshold is used to compute the global threshold. I convert
% floating point images to uint8 prior to computing the image histogram to
% avoid issues with NaN/Inf values in the input data. im2uint8 nicely
```

```
% handles these so that I get a clean histogram for otsuthresh. For other
% types, I compute the histogram in the native type, using 256 bins (this
% is the default in imhist).
if isfloat(I)
    I = im2uint8(I);
    T = otsuthresh( imhist(I) );
else
    T = otsuthresh( imhist(I) );
end
end
%--------------------------------------------------------------------------
% Input Parsing
%--------------------------------------------------------------------------
function [I,isNumericThreshold,options] = parseInputs(I, varargin)
% validate image
validateImage(I);
isNumericThreshold = ~isempty(varargin) && ~ischar(varargin{1});
if isNumericThreshold
    options.T = validateT(varargin{1},size(I));
    if numel(varargin)>1
        error(message('MATLAB:TooManyInputs'))
    end
else
    if isempty(varargin)
        options.Method = 'global';
        return;
    end

    options.Method = validatestring(varargin{1},{'global','adaptive'},mfilename,'Method',2);
    if strcmp(options.Method,'global')
        if numel(varargin)>1
            error(message('MATLAB:TooManyInputs'))
        end
    else
        options.Sensitivity = 0.5;
        options.ForegroundPolarity = 'bright';
        numPVArgs = numel(varargin)-1;
        if mod(numPVArgs,2)~=0
            error(message('images:validate:invalidNameValue'));
        end

        ParamNames = {'Sensitivity','ForegroundPolarity'};
        ValidateFcn = {@validateSensitivity,@validateForegroundPolarity};

        for p = 2 : 2 : numel(varargin)-1
            Name = varargin{p};
            Value = varargin{p+1};
            idx = strncmpi(Name, ParamNames, numel(Name));

            if ~any(idx)
                error(message('images:validate:unknownParamName', Name));
            elseif numel(find(idx))>1
                error(message('images:validate:ambiguousParamName', Name));
            end
            validate = ValidateFcn{idx};
            options.(ParamNames{idx}) = validate(Value);
        end
    end
end
end
```

```
function validateImage(I)
supportedClasses = {'uint8','uint16','uint32','int8','int16','int32','single','double'};
supportedAttribs = {'real','nonsparse','2d'};
validateattributes(I,supportedClasses,supportedAttribs,mfilename,'I');
end

function T = validateT(T,sizeI)
validateattributes(T,{'numeric'},{'real','nonsparse','2d'},mfilename,'Threshold',2);
if ~( isscalar(T) || isequal(size(T),sizeI) )
    error(message('images:imbinarize:badSizedThreshold'))
end
end

function s = validateSensitivity(s)
validateattributes(s,{'numeric'},{'real','nonsparse','scalar','nonnegative','<=',1},mfilename,
'Sensitivity');
end

function fgp = validateForegroundPolarity(fgp)
fgp = validatestring(fgp,{'bright','dark'},mfilename,'ForegroundPolarity');
end
function I = rgb2gray(X)
%RGB2GRAY Convert RGB image or colormap to grayscale.
%   RGB2GRAY converts RGB images to grayscale by eliminating the
%   hue and saturation information while retaining the
%   luminance.
%
%   I = RGB2GRAY(RGB) converts the truecolor image RGB to the
%   grayscale intensity image I.
%
%   NEWMAP = RGB2GRAY(MAP) returns a grayscale colormap
%   equivalent to MAP.
%
%   Class Support
%   -------------
%   If the input is an RGB image, it can be uint8, uint16, double, or
%   single. The output image I has the same class as the input image. If the
%   input is a colormap, the input and output colormaps are both of class
%   double.
%
narginchk(1,1);
[X, threeD] = parse_inputs(X);
if threeD
  I = images.internal.rgb2graymex(X);
else
  % Calculate transformation matrix
  T    = inv([1.0 0.956 0.621; 1.0 -0.272 -0.647; 1.0 -1.106 1.703]);
  coef = T(1,:);
  I = X * coef';
  I = min(max(I,0),1);
  I = [I,I,I];
end
%%%
%Parse Inputs
%%%
function [X, threeD] = parse_inputs(X)
threeD = (ndims(X)==3);
if (threeD)
    if ((size(X,3) ~= 3))
      error(message('MATLAB:images:rgb2gray:invalidInputSizeRGB'))
    end
```

```
elseif ismatrix(X)
  if (size(X,2) ~=3 || size(X,1) < 1)
    error(message('MATLAB:images:rgb2gray:invalidSizeForColormap'))
  end
  if ~isa(X,'double')
    error(message('MATLAB:images:rgb2gray:notAValidColormap'))
  end
else
  error(message('MATLAB:images:rgb2gray:invalidInputSize'))
end
%no non-numeric arrays
if ~isnumeric(X)
  error(message('MATLAB:images:rgb2gray:invalidType'))
end
function im = imcomplement(im)
%IMCOMPLEMENT Complement image.
%   IM2 = IMCOMPLEMENT(IM) computes the complement of the image IM.  IM
%   can be a binary, intensity, or truecolor image.  IM2 has the same class and
%   size as IM.
%
%   In the complement of a binary image, black becomes white and white becomes
%   black.  For example, the complement of this binary image, true(3), is
%   false(3).  In the case of a grayscale or truecolor image, dark areas
%   become lighter and light areas become darker.

validateattributes(im,...
    {'logical','numeric'},...
    {'nonsparse'},...
    'imcomplement');

if(~isreal(im) && ~isa(im,'double'))
    % Only double valued complex images are supported for backwards
    % compatibility.
    error(message('images:imcomplement:complexInput'));
end

if(islogical(im))
    im = ~im;

elseif(isa(im,'uint8')      || isa(im,'uint16') ...
        || isa(im,'uint32') || isa(im,'uint64'))
    im = intmax(class(im)) - im;

elseif(isa(im,'int8')       || isa(im,'int16') ...
        || isa(im,'int32')  || isa(im,'int64'))
    im = bitcmp(im);

else
    % should be a float
    im = 1 - im;

end
```

REFERENCES

[1] J. Li, B. E. F. De Ávila, W. Gao, L. Zhang, and J. Wang, "Micro/nanorobots for Biomedicine: Delivery, surgery, sensing, and detoxification," *Sci. Robot.*, vol. 2, no. 4, pp. 1–10, 2017.

[2] S. Jeon, G. Jang, H. Choi, and S. Park, "Magnetic Navigation System With Gradient and Uniform Saddle Coils for the Wireless Manipulation of Micro-Robots in Human Blood Vessels," vol. 46, no. 6, pp. 1943–1946, 2010.

[3] L. O. Mair *et al.*, "Magnetically aligned nanorods in alginate capsules (MANiACs): Soft matter tumbling robots for manipulation and drug delivery," *Micromachines*, vol. 10, no. 4, 2019.

[4] M. Turan *et al.*, "Biomedical Applications of Untethered Mobile Milli/Microrobots," *Proc. IEEE*, vol. 103, no. 2, pp. 205–224, 2015.

[5] Y. H. Baea and K. Parkb, "Targted drug delivery to tumors: Myths, reality, possibility," *J Control Release*, vol. 153, no. 3, pp. 198–205, 2012.

[6] S. Park, S. Y. Ko, J.-O. Park, H. Li, and G. Go, "Magnetic actuated pH-responsive hydrogel-based soft micro-robot for targeted drug delivery," *Smart Mater. Struct.*, vol. 25, no. 2, p. 027001, 2016.

[7] H. Jiang, W. Yu, M. Oscai, and B. Ziaie, "A Smart Capsule With a Hydrogel-Based pH-Triggered Release Switch for GI-Tract Site-Specific Drug Delivery," *IEEE Trans. Biomed. Eng.*, vol. 65, no. 12, pp. 2808–2813, 2018.

[8] K. Ishihara and T. Furukawa, "Intelligent microrobot DDS (drug delivery system) measured and controlled by ultrasonics." pp. 1145–1150, 2002.

[9] W. Wang, L. A. Castro, M. Hoyos, and T. E. Mallouk, "Autonomous motion of metallic microrods propelled by ultrasound," *ACS Nano*, vol. 6, no. 7, pp. 6122–6132, 2012.

[10] G. Dogangil *et al.*, "Toward targeted retinal drug delivery with wireless magnetic microrobots," *2008 IEEE/RSJ Int. Conf. Intell. Robot. Syst. IROS*, pp. 1921–1926, 2008.

[11] C. Chautems, B. Zeydan, S. Charreyron, G. Chatzipirpiridis, S. Pané, and B. J. Nelson, "Magnetically powered microrobots: a medical revolution underway?," *Eur. J. Cardio-Thoracic Surg.*, vol. 51, p. ezw432, 2017.

[12] S. Chowdhury, W. Jing, and D. J. Cappelleri, "Controlling multiple microrobots: recent progress and future challenges," *J. Micro-Bio Robot.*, vol. 10, no. 1–4, pp. 1–11, 2015.

[13] R. Singh and J. W. Lillard, "Nanoparticle-based targeted drug delivery," *Exp. Mol. Pathol.*, vol. 86, no. 3, pp. 215–223, 2009.

[14] W. Gao, J. M. Chan, and O. C. Farokhzad, "reviews pH-Responsive Nanoparticles for Drug Delivery," vol. 7, no. 6, pp. 1913–1920, 2010.

[15] S. Fusco *et al.*, "An integrated microrobotic platform for on-demand, targeted therapeutic interventions," *Adv. Mater.*, vol. 26, no. 6, pp. 952–957, 2014.

[16] S. Fusco *et al.*, "Microrobots: a new era in ocular drug delivery," *Expert Opin. Drug Deliv.*, vol. 11, no. 11, pp. 1815–1826, 2014.

[17] S. Fusco, G. Chatzipirpiridis, K. M. Sivaraman, O. Ergeneman, B. J. Nelson, and S. Pané, "Chitosan Electrodeposition for Microrobotic Drug Delivery," *Adv. Healthc. Mater.*, vol. 2, no. 7, pp. 1037–1044, 2013.

[18] Huaming Li, Jindong Tan, and Mingjun Zhang, "Dynamics Modeling and Analysis of a Swimming Microrobot for Controlled Drug Delivery," *IEEE Trans. Autom. Sci. Eng.*, vol. 6, no. 2, pp. 220–227, 2008.

[19] J. Han *et al.*, "Hybrid-Actuating Macrophage-Based Microrobots for Active Cancer Therapy," *Sci. Rep.*, vol. 6, no. June, pp. 1–10, 2016.

[20] P. Erkoc, I. C. Yasa, H. Ceylan, O. Yasa, Y. Alapan, and M. Sitti, "Mobile Microrobots for Active Therapeutic Delivery," *Adv. Ther.*, vol. 2, no. 1, p. 1800064, 2019.

[21] D. De Lanauze, O. Felfoul, J. P. Turcot, M. Mohammadi, and S. Martel, "Three-dimensional remote aggregation and steering of magnetotactic bacteria microrobots for drug delivery applications," *Int. J. Rob. Res.*, vol. 33, no. 3, pp. 359–374, 2014.

[22] Y. Bae, W. D. Jang, N. Nishiyama, S. Fukushima, and K. Kataoka, "Multifunctional polymeric micelles with folate-mediated cancer cell targeting and pH-triggered drug releasing properties for active intracellular drug delivery," *Mol. Biosyst.*, vol. 1, no. 3, pp. 242–250, 2005.

[23] Y. Bae, S. Fukushima, A. Harada, and K. Kataoka, "Design of environment-sensitive supramolecular assemblies for intracellular drug delivery: Polymeric micelles that are responsive to intracellular pH change," *Angew. Chemie - Int. Ed.*, vol. 42, no. 38, pp. 4640–4643, 2003.

[24] W. Jing and D. Cappelleri, "A Magnetic Microrobot with in situ Force Sensing Capabilities," *Robotics*, vol. 3, no. 2, pp. 106–119, 2014.

[25] W. Jing and D. J. Cappelleri, "Incorporating in-situ force sensing capabilities in a magnetic microrobot," *IEEE Int. Conf. Intell. Robot. Syst.*, no. Iros, pp. 4704–4709, 2014.

[26] W. Jing *et al.*, "A microforce-sensing mobile microrobot for automated micromanipulation tasks," *IEEE Trans. Autom. Sci. Eng.*, vol. 16, no. 2, pp. 518–530, 2019.

[27] J. Nam, S. Jeon, S. Kim, and G. Jang, "Crawling microrobot actuated by a magnetic navigation system in tubular environments," *Sensors Actuators, A Phys.*, vol. 209, pp. 100–106, 2014.

[28] R. Sahai, S. Avadhanula, R. Groff, E. Steltz, R. Wood, and R. S. Fearing, "Towards a 3g crawling robot through the integration of microrobot technologies," *Proc. - IEEE Int. Conf. Robot. Autom.*, vol. 2006, no. May, pp. 296–302, 2006.

[29] Wei Zhang, Shuxiang Guo, and Kinji Asaka, “Developments of two novel types of underwater crawling microrobots,” *IEEE Int. Conf. Mechatronics Autom. 2005*, vol. 4, no. July, pp. 1884–1889, 2006.

[30] L. Chaodong and H. Xiaojing, “A bio-mimetie pipe crawling microrobot driven based on self-excited vibration,” *2007 IEEE Int. Conf. Robot. Biomimetics, ROBIO*, no. 1, pp. 984–988, 2007.

[31] X. Zhao, S. A. Chester, H. Yuk, R. Zhao, and Y. Kim, “Printing ferromagnetic domains for untethered fast-transforming soft materials,” *Nature*, vol. 558, no. 7709, pp. 274–279, 2018.

[32] K. E. Peyer, L. Zhang, and B. J. Nelson, “Bio-inspired magnetic swimming microrobots for biomedical applications,” *Nanoscale*, vol. 5, no. 4, pp. 1259–1272, 2013.

[33] T. Xu, G. Hwang, N. Andreff, and S. Regnier, “The rotational propulsion characteristics of scaled-up helical microswimmers with different heads and magnetic positioning,” *2013 IEEE/ASME Int. Conf. Adv. Intell. Mechatronics Mechatronics Hum. Wellbeing, AIM 2013*, pp. 1114–1120, 2013.

[34] G. Kósa, M. Shoham, and M. Zaaroor, “Propulsion method for swimming microrobots,” *IEEE Trans. Robot.*, vol. 23, no. 1, pp. 137–150, 2007.

[35] W. Hu, G. Z. Lum, M. Mastrangeli, and M. Sitti, “Small-scale soft-bodied robot with multimodal locomotion,” *Nature*, vol. 554, no. 7690, pp. 81–85, 2018.

[36] J. Xiao, J. Z. Xiao, N. Xi, R. L. Tummala, and R. Mukherjee, “Fuzzy controller for wall-climbing microrobots,” *IEEE Trans. Fuzzy Syst.*, vol. 12, no. 4, pp. 466–480, 2004.

[37] X. Tang, D. Zhang, Z. Li, and J. Chen, “An omni-directional wall-climbing microrobot with magnetic wheels directly integrated with electromagnetic micromotors,” *Int. J. Adv. Robot. Syst.*, vol. 9, 2012.

[38] R. Pieters, H. Tung, S. Charreyron, D. F. Sargent, and B. J. Nelson, “RodBot : a Rolling Microrobot for Micromanipulation,” *2015 IEEE Int. Conf. Robot. Autom.*, pp. 4042–4047, 2015.

[39] J. Ali *et al.*, “Fabrication and magnetic control of alginate-based rolling microrobots,” *AIP Adv.*, vol. 6, no. 12, 2016.

[40] M. T. Hou, H. M. Shen, G. L. Jiang, C. N. Lu, I. J. Hsu, and J. A. Yeh, “A rolling locomotion method for untethered magnetic microrobots,” *Appl. Phys. Lett.*, vol. 96, no. 2, pp. 94–97, 2010.

[41] G. L. Jiang *et al.*, “Development of rolling magnetic Microrobots,” *J. Micromechanics Microengineering*, vol. 20, no. 8, 2010.

[42] S. M. Jeon, J. K. Nam, K. Choi, and G. H. Jang, “A self-positioning and rolling magnetic microrobot on arbitrary thin surfaces,” *J. Appl. Phys.*, vol. 115, no. 17, pp. 2012–2015, 2014.

[43] X. Zhang, J. Zhao, Q. Zhu, N. Chen, M. Zhang, and Q. Pan, “Bioinspired Aquatic Microrobot Capable of Walking on Water Surface Like a Water Strider,” pp. 2630–2636, 2011.

[44] T. Li *et al.*, "Janus Microdimer Surface Walkers Propelled by Oscillating Magnetic Fields," *Adv. Funct. Mater.*, vol. 28, no. 25, pp. 1–9, 2018.

[45] T. Ebefors, J. U. Mattsson, E. Kälvesten, and G. Stemme, "a Walking Silicon Micro-Robot Kth-S," pp. 1202–1205, 1999.

[46] D. Vogtmann, R. St Pierre, and S. Bergbreiter, "A 25 MG magnetically actuated microrobot walking at > 5 body lengths/sec," *Proc. IEEE Int. Conf. Micro Electro Mech. Syst.*, pp. 179–182, 2017.

[47] E. Y. Erdem *et al.*, "Thermally actuated omnidirectional walking microrobot," *J. Microelectromechanical Syst.*, vol. 19, no. 3, pp. 433–442, 2010.

[48] C. Bi, M. Guix, B. V. Johnson, W. Jing, and D. J. Cappelleri, "Design of microscale magnetic tumbling robots for locomotion in multiple environments and complex terrains," *Micromachines*, vol. 9, no. 2, pp. 1–17, 2018.

[49] W. Jing, N. Pagano, and D. J. Cappelleri, "A novel micro-scale magnetic tumbling microrobot," *J. Micro-Bio Robot.*, vol. 8, no. 1, pp. 1–12, 2013.

[50] W. Jing, N. Pagano, and D. J. Cappelleri, "A tumbling magnetic microrobot with flexible operating modes," *Proc. - IEEE Int. Conf. Robot. Autom.*, pp. 5514–5519, 2013.

[51] B. Hemes, D. Canelon, J. Dancs, and N. Papanikolopoulos, "Robotic tumbling locomotion," *Proc. - IEEE Int. Conf. Robot. Autom.*, pp. 5063–5069, 2011.

[52] U. Scarfogliero, C. Stefanini, and P. Dario, "A bioinspired concept for high efficiency locomotion in micro robots: The jumping Robot Grillo," *Proc. - IEEE Int. Conf. Robot. Autom.*, vol. 2006, no. May, pp. 4037–4042, 2006.

[53] J. Rahmer, C. Stehning, and B. Gleich, "Spatially selective remote magnetic actuation of identical helical micromachines," vol. 2845, pp. 1–10, 2017.

[54] A. Banharnsakun, T. Achalakul, and R. C. Batra, "Drug Delivery Based on Swarm Microrobots," *Int. J. Comput. Intell. Appl.*, vol. 15, no. 02, p. 1650006, 2016.

[55] G. Hwang *et al.*, "Sensors and Actuators A : Physical Mobile microrobotic manipulator in microfluidics," *Sensors Actuators A. Phys.*, vol. 215, pp. 56–64, 2014.

[56] T. Xu, J. Yu, X. Yan, H. Choi, and L. Zhang, "Magnetic actuation based motion control for microrobots: An overview," *Micromachines*, vol. 6, no. 9, pp. 1346–1364, 2015.

[57] X. Zhao, L. Li, B. Li, J. Zhang, and A. Wang, "Durable superhydrophobic/superoleophilic PDMS sponges and their applications in selective oil absorption and in plugging oil leakages," pp. 18281–18287, 2014.

[58] P. Thurgood, S. Baratchi, C. Szydzik, A. Mitchell, and K. Khoshmanesh, "Porous PDMS structures for the storage and release of aqueous solutions into fluidic environments," *Lab Chip*, vol. 17, no. 14, pp. 2517–2527, 2017.

[59] C. Yu *et al.*, "Facile Preparation of the Porous PDMS Oil-Absorbent for Oil/Water Separation," *Adv. Mater. Interfaces*, vol. 4, no. 3, 2017.

[60] C. Boehler, F. Oberueber, S. Schlabach, T. Stieglitz, and M. Asplund, "Long-Term Stable Adhesion for Conducting Polymers in Biomedical Applications: IrOx and Nanostructured Platinum Solve the Chronic Challenge," *ACS Appl. Mater. Interfaces*, vol. 9, no. 1, pp. 189–197, 2017.

[61] S. H. Kim, J. H. Moon, J. H. Kim, S. M. Jeong, and S. H. Lee, "Flexible, stretchable and implantable PDMS encapsulated cable for implantable medical device," *Biomed. Eng. Lett.*, vol. 1, no. 3, pp. 199–203, 2011.

VITA

Nahrin Nowrose has been working toward her Master of Science degree in the Electrical and Computer Engineering Department at Purdue University since August 2018. Her research focus at Purdue University has been fabricating small scale, low-cost soft magnetic microrobots for targeted drug delivery. Nahrin is originally from Pabna, Bangladesh. She attended Bangladesh University of Engineering and Technology (BUET), from where she obtained her Bachelor of Science degree in Electrical and Electronic Engineering (EEE). After completing her B.S. degree, Nahrin applied and got accepted for Master of Science program in Electrical and Computer Engineering at Purdue University. Nahrin worked as a Graduate Teaching Assistant at the department of Biomedical engineering and subsequently Graduate Assistant at the office of Diversity and Inclusion during her stay at Purdue.

After graduating from Purdue University, Nahrin plans to return to her home country, Bangladesh. She plans to join academia there to teach engineering classes while continuing her research in soft robotics and implantable devices.